Check for updates

ADVANCED ENGINEERING MATERIALS
www.aem-journal.com

Silicon Nanowires Driving Miniaturization of Microelectromechanical Systems Physical Sensors: A Review

*Mehrdad Karimzadehkhouei, Basit Ali, Masoud Jedari Ghourichaei, and Burhanettin Erdem Alaca**

The miniaturization of microelectromechanical systems (MEMS) physical sensors is driven by global connectivity needs and is closely linked to emerging digital technologies and the Internet of Things. Strong technical advantages of miniaturization such as improved sensitivity, functionality, and power consumption are accompanied by significant economic benefits due to semiconductor manufacturing. Hence, the trend to produce smaller sensors and their driving force resemble very much those of the miniaturization of integrated circuits (ICs) as described by Moore's law. In this respect, with its IC-, and MEMS-compatibility, and scalability, the silicon nanowire is frequently employed in frontier research as the sensor building block replacing conventional sensors. The integration of the silicon nanowire with MEMS has thus generated a multiscale hybrid architecture, where the silicon nanowire serves as the piezoresistive transducer and MEMS provide an interface with external forces, such as inertial or magnetic. This approach has been reported for almost all physical sensor types over the last decade. These sensors are reviewed here with detailed classification. In each case, associated technological challenges and comparisons with conventional counterparts are provided. Future directions and opportunities are highlighted.

1. Introduction

Following the footsteps of electronics, semiconductor sensors currently undergo a stage of significant miniaturization. In the field of electromechanical sensing, this trend is embodied by nanoelectromechanical systems (NEMS).[1] Fueled by the surge of connectivity needs in various platforms such as Internet of Things and Industry 4.0, sensor miniaturization is sought after as a pathway for improved sensitivity, diversified functionality, and reduced power consumption. These parameters address —to different degrees—evolving needs of a wide range of applications in consumer electronics, smart factory, environmental monitoring, point-of-care testing, and various autonomous systems.[2–4]

With this differentiation and specialization of sensing needs, the traditional market structure based on semiconductor manufacturing inevitably transformed as well. Industry response is probably reflected best by the replacement of the International Technology Roadmap for Semiconductors by the International Roadmap for Devices and Systems within the last decade. Semiconductor manufacturing has set the gold standard for sustainable technology development starting from the very first integrated circuits of the late 1950s to today's chips of single-digit nanometer linewidths. The resulting success was a unique combination of technological progress and economic benefits as described by the Moore's law, defining the second half of the 20th century as the Silicon Age.[5] It is in this regard that electronics offer invaluable inspiration and insight for the required technology development for sensors. In the specific case of nonplanar technologies, also a trademark of NEMS, there is a significant accumulation of knowledge and expertise. The best example of the amount of this effort is the two decades that took for fin field-effect transistors (FinFETs), the most significant deviation from 2D architecture, to mature and find their way into commercial products in 2011.[6] The next stage in 3D evolution now involves further sectioning of the fin into nanosheets represented by gate-all-around (GAA) transistors.[6,7] Successive technology nodes in electronics have always required increasingly extended periods and larger investments for technical maturity.[8,9] In parallel, the development of future architectures will also rely on

M. Karimzadehkhouei, B. Ali, M. Jedari Ghourichaei, B. E. Alaca
Department of Mechanical Engineering
Koç University
Rumelifeneri Yolu, Sariyer, Istanbul 34450, Turkey
E-mail: ealaca@ku.edu.tr

M. Karimzadehkhouei, B. E. Alaca
n²STAR-Koç University Nanofabrication and Nanocharacterization Center for Scientific and Technological Advanced Research
Koç University
Rumelifeneri Yolu, Sariyer, Istanbul 34450, Turkey

B. E. Alaca
Surface Science and Technology Center (KUYTAM)
Koç University
Rumelifeneri Yolu, Sariyer, Istanbul 34450, Turkey

The ORCID identification number(s) for the author(s) of this article can be found under https://doi.org/10.1002/adem.202300007.

© 2023 The Authors. Advanced Engineering Materials published by Wiley-VCH GmbH. This is an open access article under the terms of the Creative Commons Attribution-NonCommercial License, which permits use, distribution and reproduction in any medium, provided the original work is properly cited and is not used for commercial purposes.

DOI: 10.1002/adem.202300007

investment-intensive technology development, and hence, their commercialization is a mere question of time, as long as their usefulness is justified.[10] For example, despite significant research efforts, the first commercial GAA transistors still do not involve nanowires (NWs) due to technology-related challenges.[6] However, it is clear that such activity in the field of electronics will soon find a strong echo in NW-based NEMS.

NEMS sensors utilizing functional NW components represent the next stage in the miniaturization of microelectromechanical systems (MEMS)-based sensors with the basic research question revolving around the replacement of the more bulky and less sensitive transducers in MEMS with piezoresistive silicon (Si) NWs. The technological challenges are there to be addressed as discussed above and elsewhere.[11] However, the potential benefits of incorporating Si NWs justify further efforts,[12,13] which are increasingly reported in the literature. For example, NW resonators can be utilized as tiny transducers that can detect mass and force on the order of 10^{-21} g[14] and 10^{-15} N,[15] respectively. This opened up new venues for mass spectrometry[16] and electronic nose for gas analysis.[17] Furthermore, NWs also find application in conventional MEMS inertial sensors expanding their functionality and reducing power requirements.[18,19]

This work represents an attempt to define the miniaturization effort in such hybrid systems of MEMS with Si NWs, where the microscale architecture provides a movable interaction platform for external forces, such as the membrane of a pressure sensor, and Si NWs are used as highly sensitive strain gages measuring the minute displacements involved. The focus in this work is kept on Si NWs obtained through semiconductor manufacturing and related system-level technology development rather than self-assembly efforts. There are successful examples of such bottom-up Si NWs and their integration with MEMS.[20–23] However, the choice of emphasis of this study is justified by the potential of top-down fabrication in the next commercialization stage[24] thanks to the enormous amount of existing fab infrastructure, compatibility with electronics and wafer-level production and ubiquitous use of Si in conventional MEMS as a mechanical material. There are further review articles dedicated to the synthesis of Si NWs.[25–27] This article discusses first the technological challenges related to the cofabrication of microscale architecture with Si NWs in a batch-compatible fashion. The main approaches are classified and discussed next. This is followed by a critical study of various sensors, such as accelerometers, gyroscopes, microphones, magnetometers, and pressure and flow sensors, where Si NWs are utilized as the core building block for force sensing. With none of the discussed sensors currently commercialized, a future outlook with challenges and opportunities is provided at the conclusion of the work.

2. Fabrication Techniques

The batch fabrication of piezoresistive Si NWs with MEMS raises a series of challenges. Within the frame of semiconductor manufacturing, a few paths exist to address these challenges, among which two main approaches stand out. Both are depicted in **Figure 1**, where both the Si NW and the nearby higher-order structure, such as a movable MEMS component, a shuttle, are represented schematically on a silicon-on-insulator (SOI) wafer.

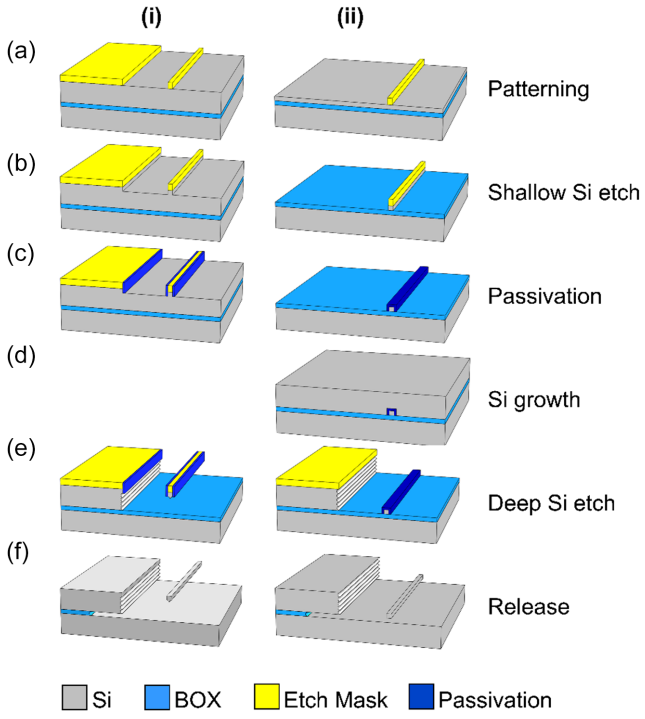


Figure 1. Column (i): An adaptation of the SCREAM process in thick SOI incorporating a two-stage etch technology and sidewall passivation.[36–40,47] Column (ii): Si NW fabrication in thin SOI with MEMS fabricated subsequently within a thick polySi layer.[18] Fabrication steps: a) patterning of etch mask by nanolithography, b) shallow Si etch to define NW partially in (i) and fully in (ii), c) passivation for protection against further Si etch, d) polySi growth in (ii) to fabricate MEMS device layer, e) deep Si etch for MEMS fabrication, and f) release through BOX etching.

The first technique, Figure 1, column (i), was developed specifically for thick SOI substrates. It represents a nanoscale version of the single-crystal reactive etching and metallization (SCREAM) process,[28] where both the NW and MEMS are fabricated within the SOI device layer in a monolithic fashion. Originally developed for the fabrication of free-standing Si micromechanical structures within bulk Si substrates,[29–35] the technique was recently extended into the nanoscale.[36–40] Using a two-stage etching technique, NWs are obtained at the upper surface of the device layer, i.e., coplanar with the MEMS surface.

The second technique, Figure 1, column (ii), works on thin SOI substrates. While the Si NW is generated within the thin device layer, MEMS is subsequently fabricated within a thick polycrystalline silicon (polySi) layer deposited at a later stage.[18] As opposed to column (i), a further lithographic step is required to pattern MEMS before a deep etch process is carried out. The resulting Si NW is thus attached to the bottom of MEMS.

SCREAM is a surface micromachining tool introduced to obtain micromechanical structures within bulk Si crystal.[28] Various applications, such as Si scanning probes[41] and Si MEMS,[29,42] benefited from the technology without any need for SOI substrates. Its adaptation at the nanoscale as depicted in Figure 1, column (i), proved to enable monolithic cofabrication of the Si NWs. Si NWs with a critical dimension (CD) of 20 nm could be obtained after a 10 μm-deep etch step, thereby bridging

© 2023 The Authors. Advanced Engineering Materials published by Wiley-VCH GmbH

15272648, 2023, 12, Downloaded from https://onlinelibrary.wiley.com/doi/10.1002/adem.202300007 by Turkey Cochrane Evidence Aid, Wiley Online Library on [20/02/2025]. See the Terms and Conditions (https://onlinelibrary.wiley.com/terms-and-conditions) on Wiley Online Library for rules of use; OA articles are governed by the applicable Creative Commons License

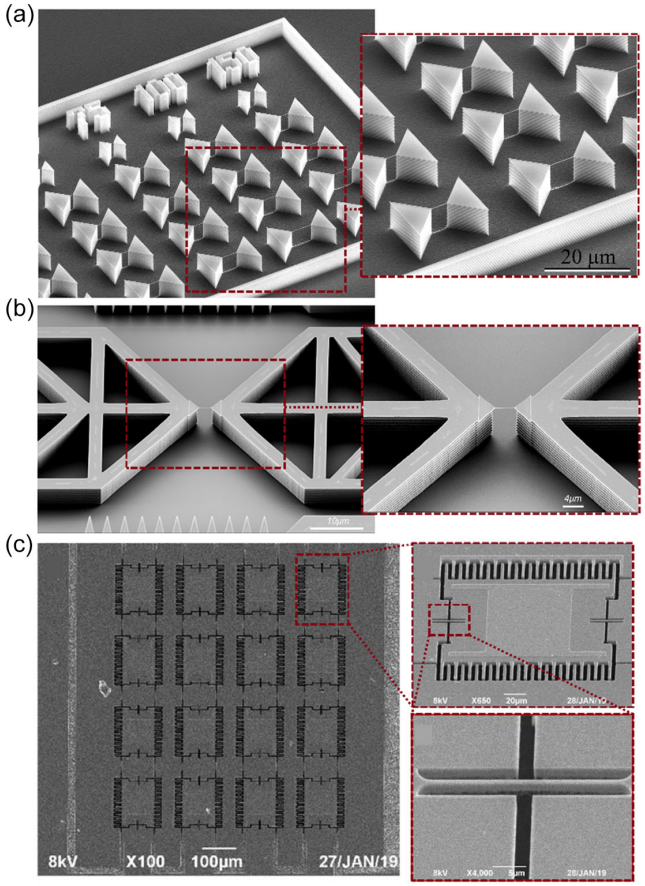


Figure 2. a) Monolithic batch fabrication of the Si NWs with an etch depth of 10 μm within bulk Si. Reproduced with permission.[43] Copyright 2016, IOP Publishing, Ltd. b) Integration of a Si NW (in the middle) and MEMS (as bulky shuttles at both ends of the NW) within a 10 μm-thick SOI device layer. Reproduced with permission.[46] Copyright 2017, American Vacuum Society. c) A micromirror array incorporating 5 μm-thick plates suspended by NWs with a CD of 1 μm. Reproduced with permission.[45] Copyright 2020, IEEE.

a three-order-of-magnitude scale gap.[39,43] An array of such Si NWs fabricated within bulk Si is depicted in **Figure 2**a, where all features were monolithically machined from the same Si crystal. An etch depth as large as 40 μm was later demonstrated, indicating the promising aspects of the technology for multiscale integration.[44] An example of the resulting MEMS integration in thick SOI is also depicted in Figure 2b, which shows a MEMS stretcher with a NW bridging two 10 μm-thick end-effectors, representing the state of the art of monolithic precision achieved through semiconductor processing. The stretcher was later used to measure piezoresistive gage factors.[19] Similarly, Figure 2c shows a 4×4 array of micromirrors incorporating $100 \times 100\ \mu m^2$ square plates with a thickness of 5 μm. These thick plates are suspended by NW springs of a CD of 1 μm. This device is proposed as a high-performance spatial light modulator with a high resonance frequency, good mechanical reliability, and large deflection angles.[45]

The associated process in its most generic form involves the following steps (Figure 1, column (i)):

Fabrication starts with the lithographic definition of an etch mask (step a). This involves mix-and-match lithography for patterning at multiple scales. Although further processes such as metallization through lift-off[46] and selective doping[37] raise the need for extra lithographic steps, the definition of the etch mask here represents the essential patterning need. It is during this stage that the NW width and length are defined as well as its placement with respect to MEMS. Multiscale production will benefit from high-resolution lithography such as extreme ultraviolet lithography (EUV)[47–49] or mix-and-match lithography[50,51] as both enable the cofabrication of both nano- and microscale components.

This is followed by the first Si etch step (step b). This shallow etch is achieved through reactive ion etching (RIE) with chlorine chemistry and its depth defines the height of the Si NW. Side-wall passivation (step c) is implemented through low-temperature oxide (LTO) deposition.[43] Other oxides, such as tetraethyl orthosilicate (TEOS),[37] thermal oxide,[40] and low-pressure chemical vapor deposited (LPCVD) oxide,[47] were also used as the passivation material.

The passivation layer is then removed from horizontal surfaces through RIE. This is followed by the final Si etch step, a deep etch with fluorine chemistry[46] (step e). While this etch defines the MEMS layer, the Si NW is also released as a free-standing feature during this stage. This release step is made possible by the fact that the NW CD is considerably smaller than the extent of undercuts due to etch scallops, and hence, all Si from underneath the NW can be removed. As the extent of scallops is negligible compared to MEMS dimensions, no further measure is necessary for obtaining both micro- and nanoscale features during this single deep etch process. Finally, MEMS release is carried out in hydrofluoric acid (HF) (step f). Both vapor phase[39] and liquid[47] etching were reported previously for this purpose.

As the NW bottom surface is formed during the deep etch step, scallops have a direct influence on NW cross-sectional features. With an increasing radius of curvature of scallops with respect to the NW CD, the NW bottom surface becomes increasingly smooth.[43] The presence of gate electrodes placed in the vicinity of the NWs also leads to a certain extension of the NW at its bottom, whose evolution is well documented as a function of etch depth.[44] The deep etch step was also shown not to alter the NW crystal structure[52] nor to induce significant intrinsic stresses.[53]

Instead of releasing the NW through the scalloping effect, some studies carried out the deep etch without any NW release. This approach results in a Si column underneath the NW with only the upper part protected by the side-wall passivation layer. To release the NW, the lower part of this Si column is then removed via anisotropic wet etch using ethylenediamine pyrocatechol (EDP),[54] tetramethylammonium hydroxide (TMAH),[47] or potassium hydroxide (KOH).[40] Alternatively, isotropic Si etching can also be employed to release the NW as reported previously.[38] In this case, the thickness of the initial protrusion of step b is partly consumed, and hence, the extent of the prior shallow etch process should be carefully adjusted. The technique was demonstrated later in the case of an electrostatic micromirror array, where the NWs serve as torsional springs shown previously in Figure 2c.[45]

© 2023 The Authors. Advanced Engineering Materials published by Wiley-VCH GmbH

15272648, 2023, 12, Downloaded from https://onlinelibrary.wiley.com/doi/10.1002/adem.202300007 by Turkey Cochrane Evidence Aid, Wiley Online Library on [20/02/2025]. See the Terms and Conditions (https://onlinelibrary.wiley.com/terms-and-conditions) on Wiley Online Library for rules of use; OA articles are governed by the applicable Creative Commons License

Alternatively, instead of the lithographic definition of the etch mask involving mix-and-match lithography steps, Si NWs can be patterned via focused ion beam (FIB) implantation. Followed by etching of undoped Si, Si NWs are obtained. Either isotropic or crystal orientation-dependent, selective wet etch by KOH,[55–58] TMAH,[59–67] or anisotropic dry etch by RIE,[68] or DRIE[69] are used for this purpose.

The alternative process in Figure 1, column (ii), introduced in 2009[18] follows similar generic steps as those described for column (i). The main difference is the use of a thin SOI substrate with initial demonstrations carried out with a device layer thickness of 250 nm.[70] This thickness defines the NW thickness, whereas in-plane dimensions are set during the high-resolution lithography step (step a) followed by shallow etching (step b). A 0.3 μm-thick oxide layer is used for encapsulating the NW (step c). This is followed by the deposition of a 10 μm-thick polySi (step d). This layer is then patterned and etched to form the MEMS architecture (step e). The protective oxide layer along with buried oxide (BOX) is then removed by HF vapor etching (step f). The applications of this technology to a variety of sensors were reported ranging from inertial measurement devices to pressure sensors.[71–73]

Both approaches discussed so far present viable solutions to wafer-level batch processing of multiscale systems and provide a path for the future commercialization of miniaturized, sensitive, and low-power sensors. The first approach based on thick SOI provides flexibility regarding NW dimensions, as one is not limited by the SOI device layer thickness. Similarly, it can accommodate innovative approaches regarding the combination of different materials and processes. It also has the advantage of a much lower thermal budget due to the lack of any CVD growth. Finally, with the NW obtained at the top surface, the technology eliminates working with vias and enables easier integration of processes such as doping and contact formation.

3. Applications and Devices

Various sensor platforms have been reported so far that incorporate Si NWs as the central sensing element. Examples include accelerometers, gyroscopes, magnetometers, and flow and pressure sensors. This wide range of sensor applications indicates the relevance and applicability of the technology. Representative devices for each sensor type are discussed in this section.

3.1. Accelerometers

MEMS accelerometers incorporate a Si shuttle whose displacement under inertial forces is converted into an electrical signal using a capacitive or piezoresistive transduction mechanism.[74,75] By replacing the transducing element through a piezoresistive Si NW, a significant level of miniaturization can be achieved. This has two important consequences: first, a higher sensitivity is achieved by placing the NW at a location of stress concentration, thereby maximizing the piezoresistive readout. Second, miniaturization leads to higher resonance frequencies, a feature that is increasingly sought after in high-*g* applications.[76]

All Si NW-based accelerometers depicted in **Figure 3** consist of a shuttle that is suspended through mechanical flexures and piezoresistive Si NW bridges. The first design, Figure 3a, is based on the thin-SOI technology for which the fabrication process was already described in Figure 1, column (ii). This resonant accelerometer[72] involves a MEMS proof mass, *M*, with a thickness of 20 μm connected to a hinge, *H*, joined to the Si NW gages, *G*, and nanoresonators, *R*, with a CD of 250 nm each. The proof mass attached to the hinge via a lever arm, *L*, rotates around the hinge axis following the application of an inertial force, F_a. There are two nanoresonators, both oriented perpendicular to the line joining the center of the shuttle and the hinge. One end of both nanoresonators is attached to the lever arm, while the other end is fixed at an anchor, U. Each nanoresonator is perpendicularly connected to a differentially configured pair of Si NWs. These Si NWs are oriented in a direction parallel to the lever arm, with one end connected to the nanoresonator, and the other end fixed to the anchor. Any rotation of the proof mass *M* around the hinge axis as described above directly translates to the opposite, i.e., tensile and compressive, axial forces in nanoresonators. Induced axial stresses, σ_b, change the bending stiffness and, hence, shift the first-order flexural mode resonant frequency of both nanoresonators in opposite directions. Frequency sensitivity of the nanoresonators can thus be defined as the amount of shift in the first-order flexural mode resonant frequency due to the axial stresses. The perpendicular positioning of Si NWs on both sides of each nanoresonator causes a state of axial stress of the same magnitude but opposite sign in piezoresistive Si NWs due to the bending of the nanoresonators. The resistance of Si NW gages changes at the rate of the resonant frequency, thereby enabling the monitoring of any shift in nanoresonators' first-order flexural mode resonant frequency. Nanoresonators are electrostatically actuated at a frequency *f*, while the Si NWs are polarized at $f+\Delta f$ using an AC-biased voltage, essentially implementing a heterodyne detection method via a lock-in amplifier. This configuration enables the device to work in a differential manner, enhancing the output while reducing the thermal sensitivity. The resulting frequency sensitivity of the resonant accelerometer is inversely proportional to the nanoresonator width, which forms the basis of the motivation for miniaturization in resonant accelerometers.

MEMS proof mass with distinctive etch holes, the hinged support with two crossing beams, nanoresonators, and the Si NWs are visible at different magnification levels in Figure 3a. Both Si NWs and nanoresonators have a $0.25 \times 0.25\ \mu m^2$ cross section. Characterization tests were conducted in the range of ±1 g with a vacuum-sealed accelerometer at room temperature. A rotating table was used to apply the acceleration, where output is proportional to the bias voltage and the relative resistance change of piezoresistive Si NWs. The resonance frequency of the nanoresonator was estimated to be 14.04 MHz, with its bandwidth calculated to be around 20 kHz, while the accelerometer itself was designed for a resonance frequency of 1.5 kHz. This proposed design offers improved sensitivity with a resonance frequency shift of up to 10% g^{-1} as shown in the plot of Figure 3a. In comparison with earlier reported resonant accelerometers,[77,78] this device exhibits excellent sensitivity and a substantial sensitivity-bandwidth product of 15 000% g^{-1} Hz, one of the highest reported so far. Besides, as a follow-up work,[79] resolution of the device was further enhanced by decreasing the noise density from 10 to 1.75 $\mu g^{-1}\ Hz^{-1/2}$, resulting from improved vacuum levels as a part of wafer-level packaging.

© 2023 The Authors. Advanced Engineering Materials published by Wiley-VCH GmbH

15272648, 2023, 12, Downloaded from https://onlinelibrary.wiley.com/doi/10.1002/adem.202300007 by Turkey Cochrane Evidence Aid, Wiley Online Library on [20/02/2025]. See the Terms and Conditions (https://onlinelibrary.wiley.com/terms-and-conditions) on Wiley Online Library for rules of use; OA articles are governed by the applicable Creative Commons License

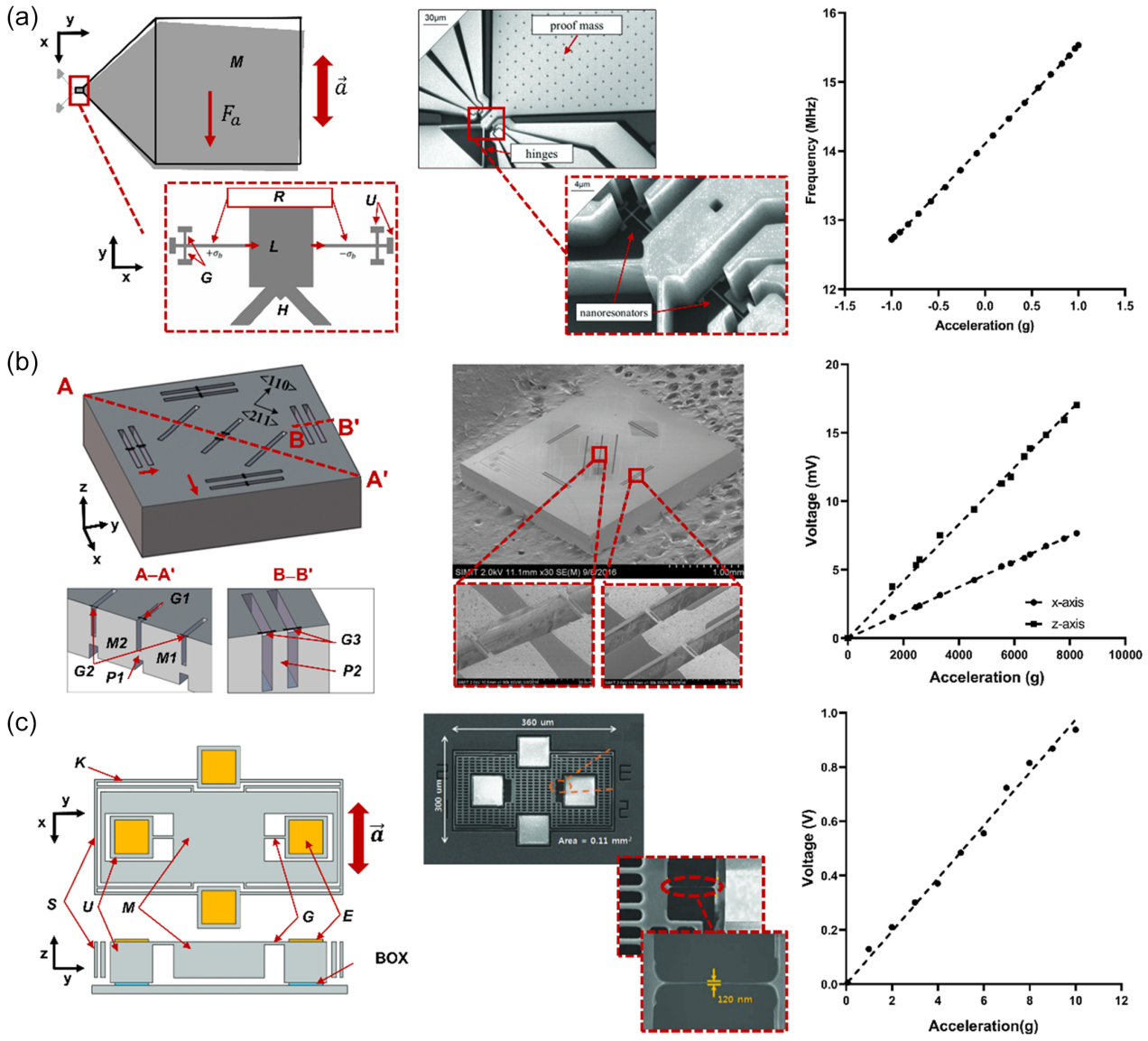


Figure 3. a) Schematic of nanoresonator-based accelerometer design. The SEM image provides a close-up with nanoresonators, *R*, connected to a differential pair of Si NW gages, *G*, on both sides of the proof mass, *M*. Sensor response in terms of resonance frequency change of nanoresonators detected through the piezoresistive Si NW gages is provided in the plot. Reproduced with permission.[72] Copyright 2020, IEEE. b) Schematic of the monolithic triaxial high-g accelerometer with insets showing cross-sectional views of out-of-plane (*A*–*A*′) and in-plane (*B*–*B*′) sensors. The SEM image depicts Si NW gages used for both axes. Sensor output for both axes is presented in the right panel. Reproduced with permission.[47] Copyright 2017, IOP Publishing, Ltd. c) Schematic of the accelerometer design incorporating two Si NW piezoresistors, *G*, for differential measurement. The SEM image shows the fabricated device with a total area of 0.11 mm^2. A close-up of the image depicts the Si NWs suspended between the anchor and shuttle, *M*. The sensor response to acceleration is plotted up to 10 g in the right panel. Reproduced with permission.[40] Copyright 2019, IEEE.

Another work based on similar technology was reported earlier by the same research group involving the above-described design without nanoresonators.[18] Comprised of a proof mass directly connected to the single Si NW through a lever arm, the proposed design relied on the lever-arm effect to transfer the proof mass displacement to the Si NW. The lever arm was found to amplify the induced stress in the Si NW, brought about by the movement of the proof mass when subjected to acceleration. The relatively small Si NW cross section and the amplifying effect of the lever arm effectively turned the Si NW into a stress concentration spot. The associated stress amplification factor was reported to be 30 for this design. The device had a reported resonance frequency of approximately 19 kHz with an estimated maximum acceleration range in excess of 100 g. The follow-up of this work also explored the possibility of improving the device sensitivity and reducing the thermal drift and nonlinearities by conducting differential measurements. This was achieved by using a pair of Si NWs with each Si NW located on opposite sides of the lever.[80] The proposed in-plane accelerometer design incorporated a differential

© 2023 The Authors. Advanced Engineering Materials published by Wiley-VCH GmbH

15272648, 2023, 12, Downloaded from https://onlinelibrary.wiley.com/doi/10.1002/adem.202300007 by Turkey Cochrane Evidence Aid, Wiley Online Library on [20/02/2025]. See the Terms and Conditions (https://onlinelibrary.wiley.com/terms-and-conditions) on Wiley Online Library for rules of use; OA articles are governed by the applicable Creative Commons License

measurement principle, and its fabrication technique was also equally compatible with the out-of-plane accelerometer.[71] Furthermore, various strategies for improving the bandwidth and damping performance of the device were experimentally investigated for use in a shock environment with an option for tunable bandwidth and mechanical filtering of a signal as low as 3 Hz.[81,82] Recently, the monolithic integration of the accelerometer on a single chip along with a pressure sensor was demonstrated.[71] The proposed 3-axis accelerometer realized through the fabrication of in-plane and out-of-plane uniaxial accelerometers on the same chip in combination with a pressure sensor highlights the compatibility of the fabrication process for integrating different devices on the same chip.

Another inertial measurement device of immense importance is the high-*g* MEMS accelerometer needed in pyro shock monitoring, precision-guided weapons, and blast and crash testing. Some applications such as penetration weapons involve accelerations of up to 200 000 g.[83] Under such conditions, piezoresistive transduction is preferred over capacitive transduction because of high resonance frequencies, large bandwidths, and scalability of both device sensitivity and resonant frequency to different measurement ranges.[84] The performance of high-*g* accelerometers is described by their figure of merit, $\Phi = S\omega^2$, which is the product of the square of the resonance frequency, ω, and sensor normalized sensitivity, S.[84] Both factors equally benefit from miniaturization to the nanoscale, as with reduced sensor size both the resonance frequency and sensitivity to physical perturbations increase. This miniaturization is directly reflected by the evolution of the accelerometer architecture over the years. High-*g* piezoresistive accelerometers can be classified as having embedded, bridge, and NW-based transducer architecture according to the piezoresistor geometric configuration.[11] The embedded configuration involves piezoresistors planted within the proof mass by doping silicon surface at locations of maximum strain.[85,86] On the other hand, bridge configuration entails proof mass anchored to the supports through a released piezoresistive structure, where any movement of the proof mass results in direct axial deformation of this bridge.[84,87,88] The third and final architecture involves further thinning of the bridge in the form of a Si NW.[47,54] Compared to the embedded architecture, the bridge-type or NW-based configurations offer independent optimization of the proof mass and piezoresistive geometry. This results in enhanced efficiency of transduction and sensitivity improvement. Moreover, the resulting sensor miniaturization also leads to higher resonance frequencies due to the overall size reduction. All these factors culminate into a multiple-order-of-magnitude improvement of the figure of merit, Φ. A broad review of the effect of piezoresistor CD on Φ demonstrated by various high-*g* accelerometers corroborates the merits of miniaturization.[11] Compared to conventional accelerometers, high-*g* sensing still remains a niche field.[76,89] However, it is clearly evident that both types of accelerometers can equally benefit from miniaturization.

A recent Si NW-based triaxial high-*g* accelerometer[47] is shown in Figure 3b. It was fabricated through a modified thick-SOI process as laid out in Figure 1, column (i). Conventional triaxial shock sensors are prepared by mounting three independent uniaxial sensors onto a single platform; however, the adapted practice is prone to alignment errors adversely affecting the accuracy. On the other hand, monolithic triaxial high-*g* accelerometers usually suffer from relatively lower *z*-axis resonance frequencies, as compared to their in-plane counterparts. As this practically limits the bandwidth,[87] a monolithic triaxial high-*g* accelerometer was proposed offering approximately similar resonance frequencies for in-plane and out-of-plane axes. The schematic in Figure 3b depicts the accelerometer design, with the *z*-axis sensor located at the chip center surrounded by in-plane sensors along four edges. Sensitive axes of in-plane sensors are indicated by red arrows. Cross-sectional views of the out-of-plane and in-plane sensors are represented as A–A' and B–B' sketches in the inset, respectively.

z-axis sensor (A–A') includes two mass blocks, $M1$ and $M2$, coupled by connection plates, $P1$. Two sets of transversely suspended Si NW gages are employed: a single Si NW gage, $G1$, connecting $M1$ and $M2$, and another pair of Si NW gages, $G2$, connecting $M1$ and $M2$ to the substrate on both sides. The connection plate, $P1$, provides the required bending stiffness under *z*-axis acceleration. On the contrary, the *x*- and *y*-axis sensors (B–B') involve partly clamped half-plate geometry with trenches etched on both sides of plate $P2$, which is connected to the substrate through a Si NW gage, $G3$, across each trench. Similar to $P1$ in the case of *z*-axis acceleration, the stiffness of $P2$ defines the sensitivity of in-plane accelerometers. Any acceleration translates into axial deformation of the corresponding Si NW gages. Each of the sensing axes involves four identical Si NWs, two in tension and the remaining two in compression. For example, in the case of the *z*-axis sensor, the z component of acceleration leads to tension in $G1$ and compression in $G2$. In-plane sensors operate in a similar fashion. Stresses of opposite signs obtained symmetrically within the accelerometer thus enable differential sensing, reducing thermal sensitivity and nonlinearity.

SEM image of Figure 3b provides close-ups of Si NW gages of both types with a CD of 3 μm. The resonance frequency for this device was reported to be around 1.4 MHz for all three axes. A commercial shock exciter was used for the device characterization that involves an accelerating metal bar under pneumatic action striking a base hosting the accelerometer. Measured data shown in the plot of Figure 3b indicate a sensitivity of 0.188 and 0.408 $\mu V\,V^{-1}\,g^{-1}$ for the *x*- and *z*-axes, respectively. The figure of merit, Φ, for the *x*- and *z*-axes were found to be 2.85×10^6 and $1.512 \times 10^6\,m^{-1}$, respectively, representing a significant improvement for high-*g* accelerometers.[11]

Several efforts have been dedicated in the past to enhance both the sensitivity and resonant frequency of the accelerometer in order to achieve a higher figure of merit. One of the approaches[90,91] involves utilizing hinges attached to proof mass as springs, to enhance the resonant frequency, while a piezoresistive bridge structure is connected to proof mass for higher sensitivity. However, with hinges used as springs, the design suffered from poor structural stability owing to the stress concentration in the joint between the proof mass and spring.[54] To address this issue while maintaining a similar performance, a new design was proposed which incorporated an additional plate spring attached to proof mass while utilizing released NW piezoresistors for high sensitivity.[54] This addition of plate springs was shown to prevent excessive stress concentration in joints between the proof mass and hinge while improving structural stability under high levels of shock loading. The device is reported to offer promising robustness when

© 2023 The Authors. Advanced Engineering Materials published by Wiley-VCH GmbH

15272648, 2023, 12, Downloaded from https://onlinelibrary.wiley.com/doi/10.1002/adem.202300007 by Turkey Cochrane Evidence Aid, Wiley Online Library on [20/02/2025]. See the Terms and Conditions (https://onlinelibrary.wiley.com/terms-and-conditions) on Wiley Online Library for rules of use; OA articles are governed by the applicable Creative Commons License

characterized through a shock test platform while providing shock protection of up to 3 times the designed measurement range.

Finally, the third example of Si NW-based accelerometers is shown in Figure 3c, which was also fabricated using the thick-SOI process depicted in Figure 1, column (i). The proposed process was claimed to be a simpler, scalable fabrication method for NW-based sensors compared to a thin SOI-based fabrication process.[40] A comparison of the Si NW accelerometer performance, fabricated through the proposed method, with that of commercial capacitive accelerometers was also reported.[40] The schematic in Figure 3c describes the accelerometer design composed of a proof mass, *M*, Si NW gages, *G*, a set of springs *K*, and flying bars, *S*. The proof mass is directly connected to the anchors U via Si NWs, with the sensitive axis placed perpendicular to the Si NW longitudinal axis. A set of dynamically balanced folded-beam suspensions consisting of *K* and *S* are utilized to ensure the elimination of the nonlinearity of the dynamic response. Any acceleration along the sensitive axis causes the bending of Si NW gages. The resulting resistance change is detected through readout circuit via metal pads, *E*. The fabricated device shown in the SEM image in Figure 3c involves a pair of Si NWs with a CD of 120 nm and a length of 12 μm. The total device area is $360 \times 360\ \mu m^2$ and the accelerometer exhibited a first-order resonance frequency of 30 kHz.

The experimental setup utilized for the characterization of the accelerometer included a wire-bonded accelerometer chip mounted on a printed circuit board along with two commercial MEMS accelerometers. Device characterization was performed using a shaker system with a range of up to 10 g and an Arduino Uno board along with an analog front-end chip. The output plot of Figure 3c indicates a sensitivity of 98 mV g^{-1}, a signal-to-noise ratio (SNR), and a noise density of 62.6 dB and 266 μg $Hz^{-1/2}$, respectively. A similar performance level to that of commercial sensors was thus achieved in terms of SNR and noise density with the additional benefit of a much smaller footprint. Therefore, the proposed accelerometer depicts the potential of Si NW-based sensors as a possible alternative to conventional MEMS sensors.

3.2. Gyroscopes

Gyroscopes constitute another important class of inertial sensors. They are crucial for a variety of applications including spacecraft navigation, defense, medical, automotive industry, and consumer products such as gaming consoles and cell phones.[92–95] Several gyroscopes based on Si NWs have been reported so far, with almost all fabricated through the thin-SOI process of column (ii) in Figure 1. An early example, shown in **Figure 4**a, is commonly known as the tuning fork gyroscope.[96] Its specifications are provided in row 1 of **Table 1**. This design includes two segments that are coupled by a spring, *S*, and vibrate in an antiphase mode. Each segment consists of three frames. For the *z*-axis gyroscope, these are 1) drive frame, *D*, oscillating in *x*-direction, 2) Coriolis frame, *C*, which is the proof mass, *M*, itself, of an area of $400 \times 400\ \mu m^2$, oscillating in the direction of *D* and has a degree of freedom in *y*-direction, and 3) detection frame, *F*, anchored to *D* and moving in the direction of *C*. *D* is coupled to a lever arm, *L*, that rotates about hinge support, *H*, as a result of the displacement of frame *C*. Nanogages in the form of Si NWs are symmetrically placed around *H* and monolithically attached to *L*, with their other end anchored to the substrate. By utilizing the lever arm configuration, the induced strain in Si NWs is also amplified. Driven by the capacitive actuators connected to *D*, each proof mass, *M*, vibrates out of phase with respect to its counterpart. As a result of any rotation about the *z*-axis, proof masses are displaced along the *y*-axis in opposite directions, thereby causing *F* to rotate about the *z*-axis. Due to the symmetric positioning of both Si NWs around *H*, the center of rotation, axial stresses of equal magnitude and opposite sign are generated in both Si NWs, thus enabling differential measurement. A close-up top view of a piezoresistive Si NW with a cross-sectional area of $250 \times 250\ nm^2$ is also depicted in Figure 4a.

This device demonstrates a sensitivity of 1.4×10^{-6} V dps^{-1} in *z*-axis. Its minute mass due to reduced transducer dimensions also leads to a high resonance frequency, which, in turn, facilitates further improvement in sensitivity through higher drive frame frequencies. It is worth mentioning that the motion of the drive frame, *D*, can affect that of the detection frame, *F*, resulting in unstable operation. To overcome this interference, the drive and detection frame motion can be decoupled.[97]

In addition to the *z*-axis measurement, in-plane (*y*-axis) rotation rate measurement capability was also added, as depicted in Figure 4b(i) (See Table 1, row 2 for specifications).[98] It comprises a drive frame, *D*, a Coriolis frame, *C*, and a detection frame, *F*. Proof masses, *M*, oscillate out of phase in *x*-direction. Upon rotation about the *y*-axis, the resulting Coriolis force causes both proof masses to displace in opposite directions along the *z*-axis as indicated in red and blue colors in Figure 4b(i). As a result, the lever-arm architecture, shown in the inset of Figure 4b(i), rotates about the *y*-axis and generates stresses of opposite signs in a Si NW couple. A close-up of a 5 μm-long Si NW nanogage with a cross section of $250\ nm \times 250\ nm$ is shown in Figure 4b(ii). The accompanying *z*-axis gyroscope is illustrated in Figure 4b(iii). In this configuration, *C* responds to a rotation about the *z*-axis by deflecting the detection frame, *F*, along the *y*-axis with each proof mass, *M*, moving in opposite directions. As discussed above, the lever arm, *L*, rotating about hinged support, *H*, generates stresses of opposite sign in a Si NW couple as shown in the inset of Figure 4b(iii). In comparison with the device of Figure 4a, this design incorporates several improvements such as a new hinge–lever, *H–L*, mechanism providing a more symmetrical configuration, and a two-stage decoupling approach, where several frames decouple input stimuli from the output through a sequence of successively connected frames. To address the quadrature error existing in the decoupled MEMS gyroscope design, an electrostatic quadrature nulling shown in Figure 4b(i)–(iii) is implemented in the Coriolis frame, *C*, with capacitive electrodes.

A low-pressure wafer-level encapsulation is implemented in the device of Figure 4b via a eutectic bonding process of Si–Au, resulting in further miniaturization by decreasing the occupied area.[98] Both in-plane and out-of-plane readout circuitry are based on a half Wheatstone bridge configuration with two Si NW gages and two dummy resistors, each of 2 kΩ resistance. Wheatstone bridges for both *y*- and *z*-axis devices employ similar configurations. Due to the limitations in the design, the mechanical amplification factor of the in-plane *H–L* mechanism is lower compared to that of the *z*-axis device. To compensate low

© 2023 The Authors. Advanced Engineering Materials published by Wiley-VCH GmbH

15272648, 2023, 12, Downloaded from https://onlinelibrary.wiley.com/doi/10.1002/adem.202300007 by Turkey Cochrane Evidence Add, Wiley Online Library on [20/02/2025]. See the Terms and Conditions (https://onlinelibrary.wiley.com/terms-and-conditions) on Wiley Online Library for rules of use; OA articles are governed by the applicable Creative Commons License

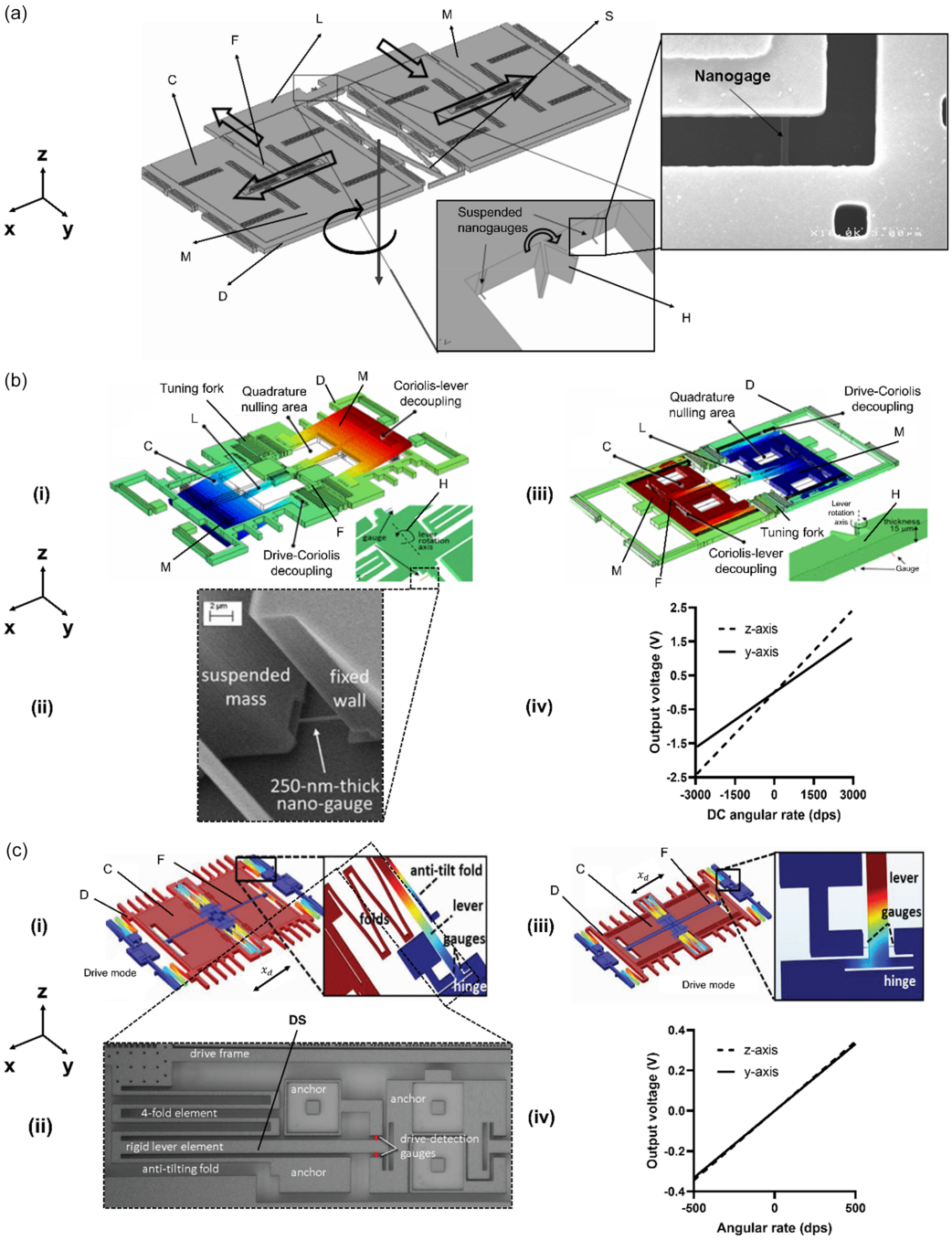


Figure 4. a) An early example of the Si NW-based *z*-axis (out-of-plane) gyroscope. The 3D model of the gyroscope shows the drive frame, *D*, Coriolis frame, *C*, detection frame, *F*, and the positions of the Si NWs as nanogages. A close-up SEM image of a Si NW is also provided. Reproduced with permission.[96] Copyright 2012, IEEE. b) A three-axis gyroscope design with a fully decoupled drive frame, *D*, and detection frame, *F*: (i) the schematic of the *y*-axis (in-plane) gyroscope, the deflected shape of Coriolis frame, *C*, shown in opposite directions as red and blue, and the positioning of Si NWs about the hinged support, *H*, (ii) the close-up SEM image of the released Si NW and its positioning in the *y*-axis device, (iii) the *z*-axis (out-of-plane) device, the deflected shape of *C* shown in opposite directions as red and blue, and the positioning of Si NWs about *H*, and (iv) the output voltage versus the full-scale range of the *y*- and *z*-axis devices has been reported and the sensitivities of 0.58 and 0.84 mV dps^{-1} are derived according to the plot. Reproduced with permission.[98,99] Copyright 2015, IEEE. c) A more recent gyroscope incorporating Si NWs serving in drive frame detection scheme and a hinge–lever, *H*–*L*, design. This design employs Si NWs rather than capacitive electrodes to detect *D* motion: (i) the positioning of the Si NWs in the *y*-axis device, and the movement direction of *D*, (ii) a close-up SEM image of Si NW gages, and the spring design of the drive frame, *D*, (iii) the positioning of the Si NWs in the *z*-axis device, and the movement direction of *D*, and (iv) the output voltage as a function of the full-scale range of *y*- and *z*-axis gyroscopes. A sensitivity of 7.5 mV dps^{-1} is obtained for both axes. Reproduced with permission.[105,106] Copyright 2017, IEEE.

© 2023 The Authors. Advanced Engineering Materials published by Wiley-VCH GmbH

15272648, 2023, 12, Downloaded from https://onlinelibrary.wiley.com/doi/10.1002/adem.202300007 by Turkey Cochrane Evidence Aid, Wiley Online Library on [20/02/2025]. See the Terms and Conditions (https://onlinelibrary.wiley.com/terms-and-conditions) on Wiley Online Library for rules of use; OA articles are governed by the applicable Creative Commons License

Table 1. Technical specifications and design parameters of Si NW-based MEMS gyroscopes.

No.	Size[a] [mm^2/axis]	Axis	NoA[b]	S[c] [V °s^{-1}]	DRF[d] [kHz]	SRF[e] [kHz]	Drive mode QF[f]	Sense mode QF	ARW[g] [° s$^{-1}\sqrt{}$Hz]	Stability [° h^{-1}]	FSR[h] [° s^{-1}]	References
1	0.5	*z*	1	1.4×10^{-6}	20.3	21.4	100 000	50 000	0.05	50	2500	[96]
2	0.349	*z*	3	0.84×10^{-3}	N/A	N/A	N/A	N/A	0.01	36	>3000	[98]
	0.316	*x* or *y*		0.58×10^{-3}					0.023			
3	0.349	*z*	3	1.86×10^{-3}	18.35	18.95	1224	N/A	0.0042	2	1000	[99]
	0.316	*x* or *y*		1.82×10^{-3}	18.43	18.83	1040		0.01			
4	1.01	*z*	3	7.5×10^{-3}	21	N/A	35 000	35 000	0.00038	N/A	1000	[105,106]
	1.13	*x* or *y*			19				N/A			
5	1.5	*z*	1	N/A	21	21.5	30 000	30 000	0.001	2	700	[109]
6	1.5	*z*	1	1.4×10^{-3}	50	50	N/A	N/A	0.00012	0.5	3000	[110]
7	1.2	*x* or *y*	1	1.3×10^{-3}	24	23.9	2000	N/A	0.0006	2.8	800	[111]

[a]Size: mechanical part size; [b]NoA: number of axis; [c]S: sensitivity; [d]DRF: drive resonance frequency; [e]SRF: sense resonance frequency; [f]QF: quality factor; [g]ARW: angle random walk; [h]FSR: full-scale range.

sensitivity of the *y*-axis device, a higher biasing voltage is needed. In the readout section, the bridge output voltage is adjusted through an instrumentation amplifier, demodulated, and finally digitized through an acquisition board. The scale factor over the angular rate between ±2950 dps is shown in Figure 4b(iv), and the sensitivity of the *y*- and *z*-axis gyroscopes is obtained as 0.58 and 0.84 mV dps^{-1}, respectively. In another effort (Table 1, row 3),[99] it has been shown that this sensitivity can be adjusted and significantly improved by manipulating bias voltage and drive frame displacement, leading to 1.82 and 1.86 mV dps^{-1} for *y*- and *z*-axis, respectively.

This device was later used to measure the earth's rotation rate.[100] The sensitivity was found to be 46 mΩ dps^{-1} with stability over more than 1000 s. Moreover, the NW-based gyroscope was compared to a capacitive gyroscope,[101] where the two gyroscopes with comparable sensitivities were exposed to the same vibration while keeping the drive displacement amplitude, noise density, and nominal mode-split value the same for both devices. Under these conditions, the NW-based gyroscope exhibited better vibration rejection compared to capacitive devices. According to Allan variance graphs, the capacitive gyroscope's angle random walk (ARW) doubled, while it remained roughly the same for the NW-based gyroscope. An analog front end (AFE) implemented for the 3-axis gyroscope demonstrated superior performance compared to the state-of-the-art AFE for available capacitive sensors in the market.[102] These devices also exhibited good reliability in a series of shock and drop tests.[103] In another effort, the device of Figure 4b was also compared to an off-the-shelf capacitive gyroscope at a sweeping frequency of up to 40 kHz. Results showed that the Si NW linearity and the piezoresistive gyroscope's compactness led to a better performance than that of its capacitive counterpart.[104]

In a more recent work depicted in Figure 4c (Table 1, row 4), capacitive sensors of the gyroscope's drive frame are replaced by Si NWs.[105,106] The operation principle of the new gyroscope is similar to that of previous generations, as it consists of the same drive frame, *D*, Coriolis frame, *C*, and detection frame, *F*, which are fully decoupled from each other. In-plane (Figure 4c(i)) and out-of-plane (Figure 4c(iii)) gyroscopes are depicted. As discussed earlier, even in fully decoupled gyroscopes, quadrature error, resulting from fabrication imperfections, still causes high bias instability and white noise.[107] To compensate for it, a quadrature nulling force could be applied in the sense direction through electrostatic electrodes. The magnitude of the nulling force is a function of drive frame motion. Capacitive electrodes are conventionally used, as shown in the gyroscope of Figure 4b, to detect the drive frame motion. It should be noted that capacitive detectors require much higher voltages during operation and dissipate more energy, thereby relying on more battery power. In the new design of Figure 4c, the capacitive drive frame detector is replaced by the Si NW that decreases the required voltage to lower than 1.8 V. Based on Figure 4c(iv), the measured sensitivity for *y*- and *z*-axis gyroscopes is about 7.5 mV dps^{-1}. Furthermore, the use of Si NWs leads to a significant reduction in the device area. Most importantly, Si NWs sensing the drive frame motion impart higher immunity to feedthrough capacitance compared to prevalent capacitive resonators and reduce temperature drift of the resistance and piezoresistive coefficient. The major challenge regarding the use of the Si NWs for drive frame detection is the magnitude of displacements that can reach values as high as 5 μm. This is considerably larger than the sense frame displacement that usually remains on the order of 10 nm. To overcome this issue, a particular drive spring, DS, design is developed connecting a rigid lever to a flexible fold (Figure 4c(ii)). This approach ensures that the strain induced in the Si NW remains in the elastic regime, and the Si NW response is linear. The aforementioned improvements as a result of using the NWs to sense drive motion can serve as a starting point for broader

© 2023 The Authors. Advanced Engineering Materials published by Wiley-VCH GmbH

15272648, 2023, 12, Downloaded from https://onlinelibrary.wiley.com/doi/10.1002/adem.202300007 by Turkey Cochrane Evidence Aid, Wiley Online Library on [20/02/2025]. See the Terms and Conditions (https://onlinelibrary.wiley.com/terms-and-conditions) on Wiley Online Library for rules of use; OA articles are governed by the applicable Creative Commons License

applications, such as vestibular implant systems that require a low-voltage operation.[108]

The frequency mismatch between the drive frame and sense frame was later increased from 300 to 500 Hz (Table 1, row 5).[109] The stability of gyroscopes was improved to $2°hr^{-1}$ over intervals up to 1000 s. More recently, the operation frequency of the *z*-axis device was increased to 50 kHz with a mismatch of up to 1.4 kHz without altering the scale factor,[110] leading to a stability of $0.5°h^{-1}$ and an improved rate random walk of $0.036\ dph\ Hz^{-1/2}$ (Table 1, row 6). The stability of the device was later improved to $0.02°h^{-1}$.[73] In the most recent work, the architecture of the *y*-axis gyroscope of Figure 4c(i) was improved, and an angle random walk of 600 $\mu dps\ Hz^{-1/2}$ was recorded, which is the lowest angle random walk ever recorded by a *y*-axis gyroscope (Table 1, row 7).[111]

3.3. Pressure Sensors

MEMS pressure sensors are one of the most ubiquitous MEMS products and have created a multibillion-dollar market with a market volume valued at nearly 2.13 billion USD in 2021.[112] These sensors predominantly find their application in the medical, aerospace, automotive, and consumer electronics sectors.[113] While measurement principles for pressure sensing have so far remained unchanged, miniaturization of the transducer element is a driving factor for an overall reduction of sensor size. This has also enabled penetration into various new domains such as the measurement of blood pressure and intraocular pressure.[113] A MEMS pressure sensor usually consists of a pressure-sensitive diaphragm that deforms when subjected to a pressure difference on both sides. This can be utilized as a differential or absolute pressure measurement tool, where the latter involves unidirectional deformation of the diaphragm with one face of the diaphragm exposed to a vacuum cavity. In both types, the diaphragm deformation can be sensed through the piezoresistive transduction mechanism. Conventional piezoresistive pressure sensors contain a pressure-sensitive diaphragm with doped Si components as embedded piezoresistors.[114] These piezoresistors are then joined in a Wheatstone bridge configuration to measure the resistance change resulting from the deflection of the diaphragm when subjected to a differential or absolute pressure drop across the diaphragm.[115]

As observed in the evolution of miniaturized accelerometers (Section 3.1), piezoresistors in pressure sensors have undergone a similar transformation, as a result of which new-generation pressure sensor designs increasingly rely on released, rather than embedded, piezoresistors. One such early example with suspended Si NWs is shown in **Figure 5**a. The fabrication method relies on a modified version of the thick-SOI process of column (i) of Figure 1. The sensor consists of a pressure-sensitive bossed square diaphragm, *D*, with each of its four sides connected to the substrate through Si NW bridges, *G*.[116] SEM images in Figure 5a depict both the 20 μm-thick diaphragm and a close-up view of a Si NW with a CD of 250 nm. A total sensor size of less than 1 mm^2 was thus achieved with the diaphragm occupying an area of $200 \times 200\ \mu m^2$.

Characterization of the device was carried out within a pressure range of 0–300 kPa using a commercial pressure measurement system as a reference. A constant-current-based measurement principle was employed to measure the voltage change across piezoresistive Si NWs. The results shown in the plot of Figure 5a reveal a linear range between 150 and 300 kPa and a pressure sensitivity of $337.5\ mV\ V^{-1}\ MPa^{-1}$. A comparison of this performance to that of a conventional diaphragm-based sensor with embedded piezoresistors reveals an almost ninefold improvement in pressure sensitivity. This design was later improved[117] by replacing the piezoresistor bridge comprised of the single Si NW with a pair of Si NWs on each side of the diaphragm. Diaphragm thickness was reduced to 6 μm and the Si NW CD was decreased to 100 nm. The resulting pressure sensitivity was found to be $495\ mV\ V^{-1}\ MPa^{-1}$ over the range of 0–100 kPa. Moreover, temperature drift was studied, and a neural network-based optimization technique was found to effectively minimize thermal-fluctuation-related errors.

The second example of a NW-based pressure sensor[118] is fabricated through a derivative of the thin SOI-based fabrication process[99] of column (ii) of Figure 1. A schematic of the device architecture is shown in Figure 5b. A square diaphragm, *D*, is anchored on an immobile frame, *F*1, on its outer edge, whereas its inner edge is guided vertically by the rigid block, *A*1. A pivot, *P*2, connects this whole structure to an outer mobile frame, *F*2, which is anchored to block, *A*2, via a pivot, *P*1, and to another block, *A*3, through Si NW gages, *G*1 and *G*2. The outer mobile frame can rotate around *P*1 and *P*2. In-plane distance between the pivots *P*1 and *P*2 is denoted by *L*, whereas d_j defines the out-of-plane distance between *A*3 and *P*1. As a result of pressure loading on *D*, *P*2 moves in *z* direction, thereby rotating *F*2 around *P*1. This rotation generates axial stresses of opposite sign in both Si NWs, *G*1 and *G*2. A stress amplification by a factor of L/d_j is thus achieved. The device employs Si NWs of a cross section of $0.25 \times 15\ \mu m^2$ with a length of 10 μm and a diaphragm radius and thickness of 40 and 0.25 μm, respectively. An SEM image of the fabricated device is shown in Figure 5b.

The device readout comprised a half Wheatstone bridge configuration, and a commercial pressure measurement system was used as a reference within a pressure range of 0–1 bar. The corresponding data are compiled in the plot of Figure 5b, exhibiting a pressure sensitivity of $6.3\ \mu V\ kPa^{-1}$. An acceptable linear response with a nonlinearity of around 0.15% full scale was measured. A sensitivity variation of less than 1% was reported during operation between 25 °C and 100 °C. The design was subsequently altered to incorporate a 3-axis accelerometer via monolithic integration.[71] The resulting device exhibited an improved sensitivity of $57.3\ \mu V\ V^{-1}\ kPa^{-1}$ with a similar nonlinearity. The temperature sensitivity of the device was further reduced to 0.06% within −35 to 145 °C. The device was later characterized at temperatures up to 522 °C.[119] Overall, the proposed piezoresistive pressure sensor with suspended Si NWs has the potential of finding application in devices that require a high-temperature operation, good resolution, low sensor footprint along with low-temperature sensitivity.

In addition to suspended NW-based pressure sensors discussed so far, a few embedded NW-based pressure sensors are also reported in the literature. One such differential pressure sensor comprises Si NWs with a CD of 100 nm embedded within a 3.5 μm-thick SiO_2 diaphragm.[120] Four pairs of Si NWs separated by 90° were embedded in a circular diaphragm with their long-axis oriented along the radial direction. A pressure

© 2023 The Authors. Advanced Engineering Materials published by Wiley-VCH GmbH

15272648, 2023, 12, Downloaded from https://onlinelibrary.wiley.com/doi/10.1002/adem.202300007 by Turkey Cochrane Evidence Add, Wiley Online Library on [20/02/2025]. See the Terms and Conditions (https://onlinelibrary.wiley.com/terms-and-conditions) on Wiley Online Library for rules of use; OA articles are governed by the applicable Creative Commons License

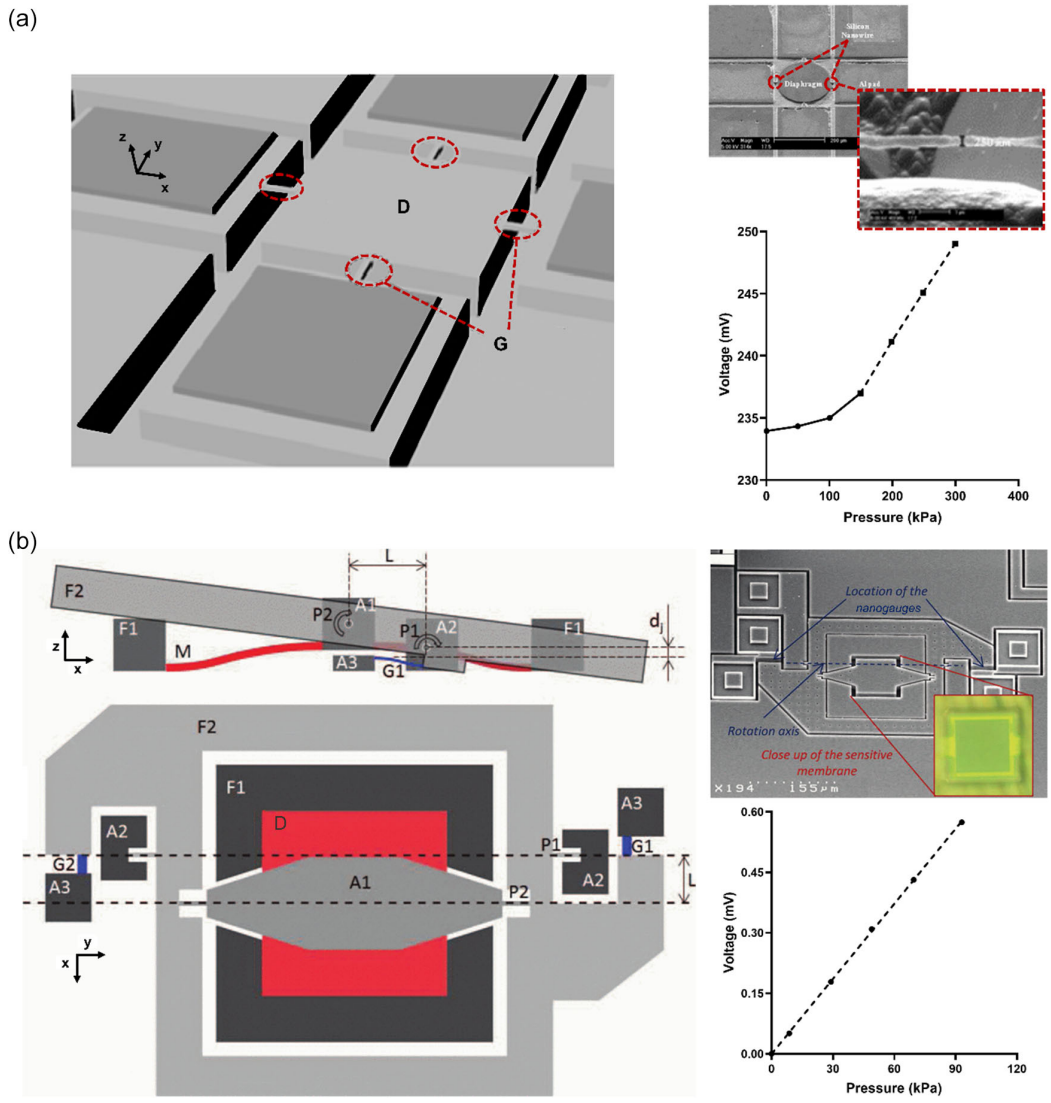


Figure 5. a) Schematic of the pressure sensor design with Si NW gages, *G*, attached to the pressure-sensitive diaphragm, *D*, on all four sides. The SEM image shows the fabricated pressure sensor with a magnified view of a piezoresistive Si NW. Measured data reveal a linear range between 150–300 kPa, marked by the dashed line. Reproduced with permission.[116] Copyright 2009, IEEE. b) Top and side views of the pressure sensor depicting a pressure-sensitive diaphragm, *D*, connected to the differential Si NW gages, *G*1 and *G*2, through a rotatable frame, *F*2. The SEM image shows the fabricated sensor. The inset shows a close-up image of the membrane. The plot exhibits the output voltage as a function of applied pressure. Reproduced with permission.[118] Copyright 2016, IEEE.

sensitivity, $\Delta RR^{-1}\Delta P^{-1}$, of 13 Pa^{-1} was achieved within the measurement range of 0–25 kPa. However, despite the high sensitivity achieved, the device suffered from a nonlinear response coupled with a low fabrication yield due to residual stresses in the SiO_2 diaphragm. A multilayered diaphragm composed of a nitride layer on top of the SiO_2 was proposed to address the output nonlinearity and fabrication yield issues.[121]

Further development of the design was made possible through an optimization of the diaphragm and BOX layer thicknesses, NW length, crystalline orientation, and doping level.[122] This, in turn, improved the device pressure sensitivity while decreasing the diaphragm deformation upon release, leading to improved fabrication yield and lower temperature sensitivity.[122] The sensitivity of the device was further enhanced by 2.5 times in the range of 0–16 kPa by introducing annular grooves on the circular diaphragm along its periphery.[123]

Finally, the latest line of work in the embedded Si NW-based pressure sensor category includes a device reported for absolute pressure measurement.[124] A pair of Si NWs is embedded in the center of each edge of a square diaphragm symmetrically, with NW orientation parallel to the edge direction. A vacuum cavity is fabricated underneath the diaphragm as a pressure reference. The device footprint is reported to be 385 μm^2. Performance characterization of the sensor revealed a nonlinearity as low as 0.31% for the range of 0-100 kPa while sensitivity fluctuations across the wafer were found to be less than 6%,[124] indicating a promising commercial prospect for similar Si NW-based pressure sensors.

© 2023 The Authors. Advanced Engineering Materials published by Wiley-VCH GmbH

15272648, 2023, 12, Downloaded from https://onlinelibrary.wiley.com/doi/10.1002/adem.202300007 by Turkey Cochrane Evidence Aid, Wiley Online Library on [20/02/2025]. See the Terms and Conditions (https://onlinelibrary.wiley.com/terms-and-conditions) on Wiley Online Library for rules of use; OA articles are governed by the applicable Creative Commons License

3.4. Microphones

MEMS microphones increasingly find application in medical devices, communication systems, and various Internet-of-Things applications.[125,126] Diaphragms are commonly used in MEMS microphones to detect sound waves based on the pressure difference between a back and a front cavity.[127] Two remarkable features of MEMS microphones are their miniaturized size and lower power consumption. For example, the reduced size of a cochlear implant microphone would ensure compactness and longer battery life.[128] As conventional microphones use a capacitive transduction scheme, their miniaturization is hampered by a series of challenges, including stiction of the backplate to the membrane, parasitic capacitance, and vulnerability to dust and humidity in the capacitive gap.[129,130] Similar to other physical sensors described so far, the replacement of the capacitive detection scheme with Si NW piezoresistors results in substantial size reduction while improving sensitivity and SNR. Specifically for MEMS microphones, the use of Si NWs leads to the elimination of the backplate, thereby avoiding back stiction and simplifying the fabrication. Hence, Si NWs have evolved into strong candidates as future transducers in MEMS microphones.

An early example of a Si NW-based microphone was reported in 2018.[131] The thin-SOI process of column (ii) of Figure 1 was used to fabricate the monolithic Si NW gages. As depicted in **Figure 6**a, the microphone comprises an inlet vent, *V*, and a back cavity, *B*, obtained through eutectic bonding between the device wafer and a second wafer (Figure 6a(i)). An in-plane deflecting beam, *D*, located next to an electrostatic actuator, *E*, (Figure 6a(ii)) is attached to a pair of identical Si NW gages, *G*, and anchored through a hinge, *H* (Figure 6a(iii)). Si NW gages have a cross-sectional area of $250 \times 250\,nm^2$. *H* is similar to the hinge used in the *z*-axis gyroscope shown in Figure 4a. Sound waves are guided through the vent, *V*, toward the deflecting beam, *D*, which oscillates in the plane of the chip due to the pressure difference between *V* and *B*. In-plane motion of the beam exerts axial loads of opposite sign on both Si NW gages, *G*, facilitating differential sensing. The electrostatic actuator, *E*, serves the purpose of verifying the full release process and evaluation of the transfer function. The resulting sensitivity was calculated between 0.1 and 0.13 $mVPa^{-1}$. Thermoelastic actuation was also implemented to induce resonance at 16.3 kHz.[131]

The technology presented in ref.[131] is also used for sub-ppm gas sensing.[132] In this design, the microphone is placed between a photoacoustic and an expansion chamber. The detection scheme is based on the absorption of specific wave lengths of a quantum cascade laser source by the target gas molecules. The modulated light of the photoacoustic chamber generates heat and thus causes a pressure difference between the two sides of the microphone diaphragm. The concentration of the gas can then be linked to diaphragm deflection thanks to Si NW gages. The performance of these sensors can be compared through Normalized Noise Equivalent Absorption (NNEA) regardless of the test condition. The value of the NNEA calculated for the micro-photoacoustic cell was found to be $3 \times 10^{-7}\,Wcm^{-1}\,Hz^{-1/2}$.

Another microphone introduced in ref.[133] includes four in-plane moving membranes and suspended Si NWs of $250 \times 250\,nm^2$ cross-sectional area placed between an anchor

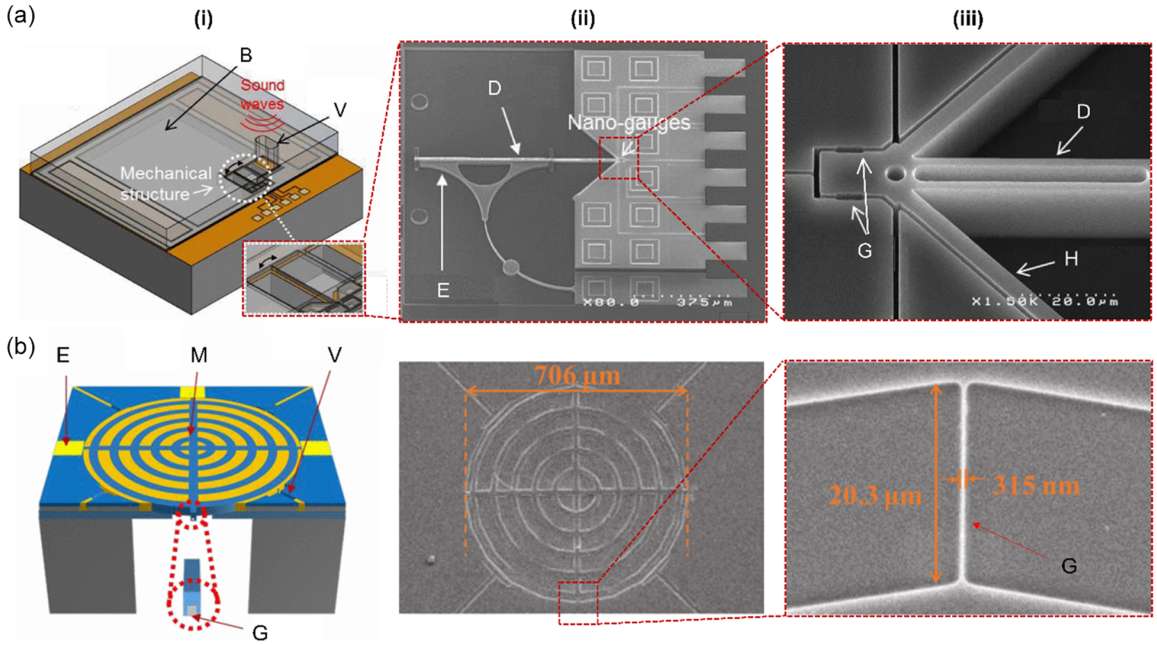


Figure 6. a) Configuration of a Si NW-based microphone: (i) Schematic of the microphone, including the inlet vent, *V*, back cavity, *B*, and a close-up view of the in-plane deflecting beam, *D*, (ii) SEM image in top view depicts the mechanical structure that comprises *D* and the electrostatic actuator, *E*, (iii) close-up SEM image showing details of deflecting beam, *D*, hinge, *H*, and Si NW gages, *G*. Reproduced with permission.[131] Copyright 2018, IEEE. b) A microphone based on thick SOI technology: (i) 3D model of the microphone reveals the positioning of the electrodes, *E*, vent holes, *V*, and a close-up view of the embedded Si NW, *G*, in the membrane, *M*, (ii) SEM image in top view depicts *M* with a diameter of 706 µm, and (iii) the close-up SEM image of *G* reveals a CD of 315 nm and a length of 20.3 µm. Reproduced with permission.[140] Copyright 2019, IEEE.

© 2023 The Authors. Advanced Engineering Materials published by Wiley-VCH GmbH

15272648, 2023, 12, Downloaded from https://onlinelibrary.wiley.com/doi/10.1002/adem.202300007 by Turkey Cochrane Evidence Aid, Wiley Online Library on [20/02/2025]. See the Terms and Conditions (https://onlinelibrary.wiley.com/terms-and-conditions) on Wiley Online Library for rules of use; OA articles are governed by the applicable Creative Commons License

and the membrane – in a similar fashion as shown in Figure 6a. In another effort, the effect of viscous turbulent perturbations at discontinuities is studied via analytical and computational techniques yielding a promising performance evaluation tool for the sensitivity and resolution of planar microphones.[134] The acoustic behavior of a similar architecture is also inspected by a vibroacoustic model based on the full linearized Navier–Stokes equations. It is found that the volume of the back cavity is the most critical parameter that affects the sensitivity.[135,136] In a subsequent study, a 0.28 µm CMOS integrated circuit is implemented as the readout circuit together with an analog-to-digital converter (ADC) based on a 1-bit Sigma delta modulator. As a result, a noise density of 7 nV $Hz^{-1/2}$ in the frequency range from 10 Hz to 10 kHz is achieved.[133,137] To increase the resolution to 95 nV $bits^{-1}$, a 65 nm CMOS integrated circuit is also used.[138] The device is recently investigated for its potential in IoT applications,[139] where a power consumption of 0.4 mW is achieved with an SNR of 77 dB and a bandwidth of 20 kHz.

An alternative approach based on the thick-SOI technology of column (i) of Figure 1 is also implemented for the fabrication of a NW-based microphone.[140] This design consists of a membrane, *M*, Si NW gages, *G*, embedded at the periphery of the membrane, electrodes, *E*, and vent holes, *V*, as depicted in Figure 6b(i). The membrane, *M*, has a diameter of 706 µm (Figure 6b(ii)). Four vent holes, *V*, are included in the design to balance the inner and outer air pressure and guide the sound waves toward the membrane, *M*, and thus create an acoustic pressure difference across *M*. The resulting membrane deflection induces strain in piezoresistive Si NW gages, *G*, a close-up of which reveals a length of 20.3 µm and a CD of 315 nm (Figure 6b(iii)). With the work focused on fabrication technology development, there are no characterization results reported yet.

3.5. Magnetometers and Flow Sensors

A magnetometer is a sensor used to detect and measure magnetic fields. Used for motion monitoring and navigation, magnetometers joined the growing list of microsensors integrated into consumer goods such as mobile phones.[141,142] The measurement principle is based on the rotation of a magnetic structure when subjected to an external magnetic field. The extent of this rotation then provides a measure of the magnetic field strength. Magnetometers are increasingly used in combination with gyroscopes and accelerometers as a part of 9-degree-of-freedom inertial measurement units (IMU).[143]

Figure 7a shows the schematic of a 3D magnetometer design, which consists of an in-plane and an out-of-plane sensor for the measurement of the magnetic field.[144] The device employs the thin-SOI technology shown in column (ii) of Figure 1. The magnetometer entails a Si-based MEMS proof mass with alternating

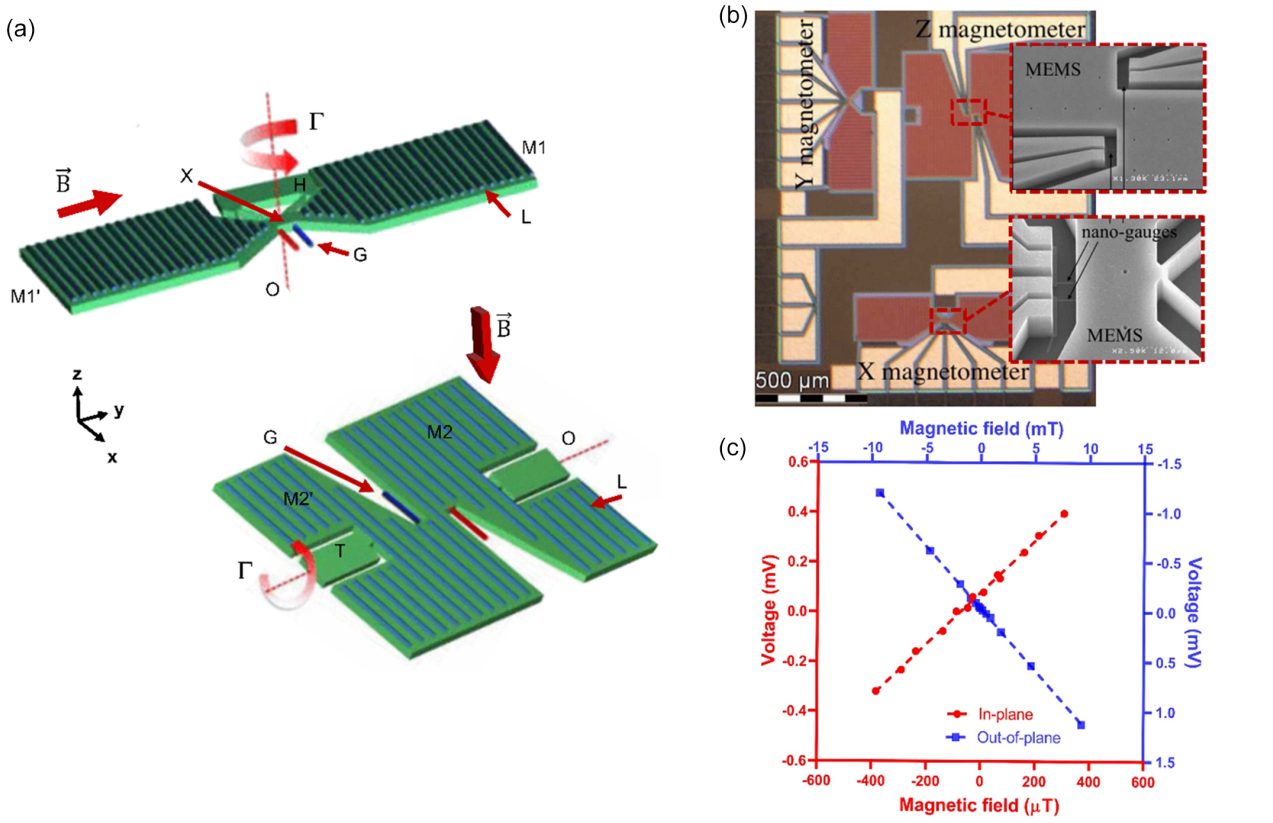


Figure 7. a) Schematic of the Si NW-based in-plane (top) and out-of-plane (bottom) magnetometer, with the applied magnetic field, $\vec{B}$, and the resultant torque, Γ, indicated by vectors. b) Micrograph of the 3D magnetometer, with the insets depicting SEM close-up images of the Si NW gages, *G* (top: in-plane, bottom: out-of-plane). c) Sensitivity plot in terms of the output voltage as a function of magnetic field for the in-plane and out-of-plane sensor. Reproduced with permission.[144] Copyright 2014, IEEE.

© 2023 The Authors. Advanced Engineering Materials published by Wiley-VCH GmbH

15272648, 2023, 12, Downloaded from https://onlinelibrary.wiley.com/doi/10.1002/adem.202300007 by Turkey Cochrane Evidence Aid, Wiley Online Library on [20/02/2025]. See the Terms and Conditions (https://onlinelibrary.wiley.com/terms-and-conditions) on Wiley Online Library for rules of use; OA articles are governed by the applicable Creative Commons License

thin layers of ferromagnetic and antiferromagnetic materials such as $Co_{80}Fe_{20}$ and PtMn, respectively. These layers are represented by blue lines, *L*, over the proof mass top surface. For the in-plane magnetometer, MEMS proof masses, *M*1 and *M*1′, are joined through a beam, X, in a symmetrical manner. X is connected to hinged support, *H*, on one side, while it is also connected to a pair of suspended Si NW gages, *G*, on the other side. With this arrangement, the entire structure assumes a see-saw configuration in the *xy* plane, which, upon the application of torque, Γ, can rotate around the axis, O, normal to the substrate plane. The amount of the applied torque depends upon the strength and direction of the external magnetic field along with the volume and magnetization of the ferromagnetic material atop the proof mass. As Si NW gages are placed symmetrically around O, they are subjected to equal axial stresses of opposite signs, as indicated by blue and red colors.

The out-of-plane design (lower sketch in Figure 7a) similarly involves connected proof masses, *M*2 and *M*2′, which are anchored to the substrate through a pair of torsional springs, T. The presence of an external out-of-plane magnetic field leads to the generation of a torque, Γ, which then rotates the proof mass about the axis, O. With Si NW gages, *G*, connected to *M*2 and *M*2′ in a symmetric fashion on opposite sides of the axis, O, they are once again subjected to equal axial stresses of opposite sign, indicated by the same color code as above.

Figure 7b shows a micrograph of the magnetometer with insets of SEM images for the in-plane and out-of-plane magnetometers. The proof mass of epitaxially grown Si has a thickness of 10 μm, while Si NW gages have a cross-sectional area of $0.25 \times 0.25\ \mu m^2$ and a length of 5 μm. MEMS fabrication is followed by the integration of magnetic materials on top of the proof mass. Alternating thin layers of ferromagnetic and antiferromagnetic materials are deposited on a tantalum seed layer through an ion-beam deposition. A tungsten nitride layer is then used for encapsulation. In order to minimize the sensitivity toward angular acceleration, the centroid of the proof mass is designed to be on the axis of rotation. A magnetic field gradient caused by the proximity of the neighboring magnetometers located on the same chip is found to have minimal effect on the sensitivity of the device.

The read-out plots are shown in Figure 7c, revealing a sensitivity of 1.09 and $0.124\ V\,T^{-1}$ with corresponding nonlinearities of 0.02% and 0.09% for the in-plane and out-of-plane magnetometers, respectively. Characterization of the device for the in-plane magnetometer was accomplished through a toroid coil by utilizing a commercial magnetometer as the calibration reference. For the out-of-plane sensor, characterization was performed through a planar coil by generating an out-of-plane magnetic field. In-plane magnetometers in *x*- and *y*-axes exhibited the same sensitivity with a reported correlation of around 99.7%. The merits of the reported work involve a miniaturized device with a reduced power consumption of 30 μW. The resolution of the device was reported to be 100 and $350\ nT\,Hz^{-0.5}$ for the in-plane and out-of-plane magnetometers, respectively, making it suitable for earth magnetic field measurement applications. Commercial IMUs are usually prepared by combining different sensor types.[143] Similar to the accelerometer and gyroscopes, the fabrication of a 3D magnetometer on a single chip is already demonstrated.[145] However, the monolithic integration of a magnetometer with a gyroscope and an accelerometer poses challenges because of the different fabrication techniques for these sensors. The current approach offers compatible fabrication of a 3D magnetometer to monolithically fabricate the magnetometers on the same chip with other inertial sensors

Flow sensors are used to measure parameters such as velocity and flow rate. They are extensively employed in consumer electronics, biomedical, automotive, and industrial sectors.[146,147] Conventional MEMS flow sensors are usually based on either the thermal[148] or mechanics-based sensing principle.[149] Thermal-based flow sensors measure the incoming flow properties via two main approaches. In the first approach, a constant thermal input is supplied to the heating element. With the flow causing a drop in the temperature of the heating element, the resulting resistance or voltage change across the heating element provides a measure of flow properties.[150,151] The second approach involves one or more than one temperature sensors installed upstream and downstream of the heating element. As the temperature of the flow changes by interacting with the heating element, this change is used to determine flow properties.[152,153] Such thermal MEMS flow sensors can be classified as thermal anemometers, calorimetric flow sensors, and time-of-flight flow sensors.[148] Mechanics-based flow sensors utilize the physical deformation of the sensor element to quantify flow properties. This deformation is caused by aerodynamic forces generated on the sensitive element of the sensor.[149,154]

With their performance directly linked to their power input, the main disadvantage of conventional MEMS thermal flow sensors is their high power consumption.[155] Moreover, sensor insulation and thermal management of the device rely on strict design limitations in order to prevent heat dissipation. Improvement of thermal insulation has been one of the approaches studied in the past via using a low-thermal-conductivity layer, free-standing structures, and a vacuum cavity beneath the heating element.[156–158] However, due to the power-intensive nature of the thermal flow sensors, the total power consumption for most thermal airflow sensors remains usually above 1 mW. On the other hand, mechanical sensors usually utilize a cantilever or a diaphragm-based architecture placed in a flow field combined with either a piezoresistive, piezoelectric, or capacitive transduction scheme to measure the flow-induced deformation of the sensing structure. While they offer low power consumption, their sensitivity and response time do not match those of thermal sensors.[158–160] As discussed previously in connection to inertial sensors, piezoresistive Si NWs raise the opportunity to enhance the performance of mechanical flow sensors. Replacing the conventional cantilever design with embedded piezoresistors by Si NW-based piezoresistors improves the sensitivity while preserving low power requirements.

Figure 8a shows the setup for the characterization of one of the few reported air flow sensors based on piezoresistive Si NWs. Si NW-based airflow sensor consists of an orifice with a diameter of 200 μm machined through an SOI wafer and a cantilever placed across the flow direction through the orifice. A pair of piezoresistive Si NWs with a CD of 90 nm are fabricated at the root of the cantilever as shown in the inset of Figure 8b. Hence, the fabrication approach resembles the thick SOI process shown in column (i) of Figure 1. Si NW gages are fabricated within the device layer of the SOI wafer, while PECVD SiO_2 and SiN_x are deposited on top to define the cantilever structure. While the bulk of the cantilever is made up of SiO_2, SiN_x layer serves the

© 2023 The Authors. Advanced Engineering Materials published by Wiley-VCH GmbH

15272648, 2023, 12, Downloaded from https://onlinelibrary.wiley.com/doi/10.1002/adem.202300007 by Turkey Cochrane Evidence Add, Wiley Online Library on [20/02/2025]. See the Terms and Conditions (https://onlinelibrary.wiley.com/terms-and-conditions) on Wiley Online Library for rules of use; OA articles are governed by the applicable Creative Commons License

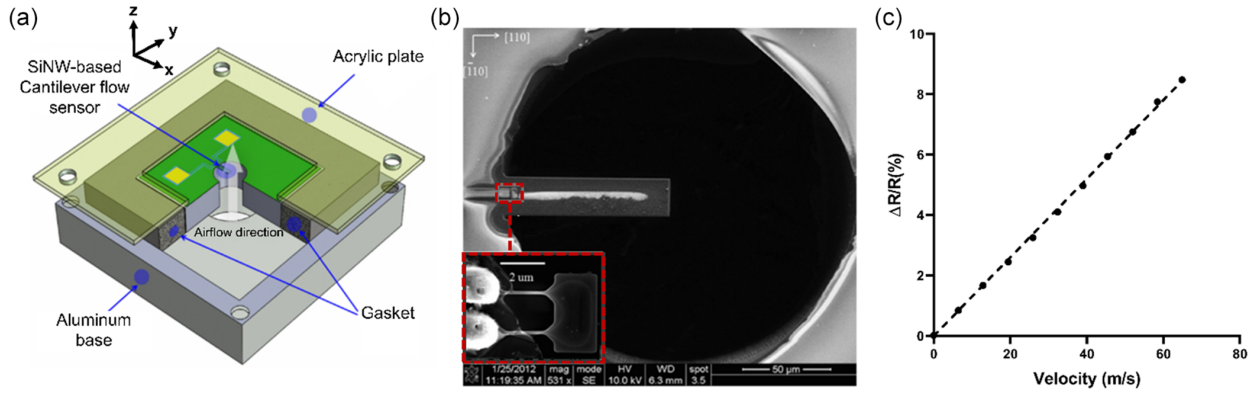


Figure 8. a) Schematic of a Si NW-based cantilever airflow sensor. b) SEM image of the cantilever air flow sensor with the cantilever placed perpendicular to the flow through an orifice visible as the black hole in the background. Inset shows a view of a Si NW pair located at the root of the cantilever beam. c) Sensor readout exhibiting a sensitivity of $1.32 \times 10^{-3}\,m^{-1}\,s$. Reproduced with permission.[155] Copyright 2012, IOP Publishing, Ltd.

purpose of counteracting unwanted initial deflection due to residual stresses within the SiO_2 layer. The device has a power consumption of less than 1 µW.[155] With the flow introduced from the back side, aerodynamic forces exerted on the cantilever deflect the cantilever. Hence, the resistance change of Si NWs due to cantilever deflection provides a direct measure of the flow velocity. Performance characterization of the device involved placing the airflow sensor inside a gasket and a hermetic sealing jig consisting of an aluminum base to avoid air leakages. The incoming air was passed through a flow meter to control the flow rate, and its pressure was measured downstream through a pressure regulator before routing it toward the flow sensor placed in the customized jig.

Figure 8b shows an SEM image of the Si NW-based airflow sensor, which employs the Si NW of 2 µm length with a cantilever size of $20 \times 90\,\mu m^2$. The Si NW resistance change as a function of the flow velocity is shown in Figure 8c, which exhibits a sensitivity value, $\Delta RR^{-1}\,V^{-1}$, of $1.32 \times 10^{-3}\,m^{-1}\,s$, where ΔRR^{-1} represents a change in the Si NW resistance normalized by initial resistance and V denotes the flow velocity. A comparison of the obtained results with earlier reported MEMS cantilever airflow sensors[161,162] reveals improved performance in terms of linearity and device sensitivity while also achieving a drastic reduction in the area. The measurement resolution was found as $1\,ms^{-1}$. Hence, the proposed Si NW-based sensor offers low-power consumption as well as improved sensitivity and linearity when compared to thermal or bulky piezoresistive MEMS flow sensors.[161–163] The superior properties of the Si NW-based airflow sensor provide yet another example of the benefits associated with the miniaturization and subsequent broad application areas for the Si NW-based piezoresistive sensors.

4. Conclusions and Outlook

The attempts to combine MEMS with Si NWs constitute an active research field as reflected by the wide range of physical sensors covered in this review. Such sensors represent a significant stage of miniaturization with a hybrid architecture, where the microscale component provides a movable platform displacing under external forces, to which Si NWs are connected as highly sensitive strain gages. This review covers almost all physical sensor types. Such ubiquitous use of Si NWs hints at their enormous potential to replace conventional sensors and it benefits from various supporting factors: 1) Despite being in its infancy for NEMS, related technology development is based on strong expertise in semiconductor manufacturing in electronics. Developments in cutting-edge 3D architectures such as gate-all-around transistors with the future prospect of utilizing NWs provide the background for wafer-scale production and hence, potential commercialization. There are parallel pathways for obtaining Si NWs and MEMS in the same device layer of SOI wafers. A classification is attempted in this review highlighting the advantages of specific technologies. A special emphasis is placed on connecting each sensor discussed to a particular technology approach. 2) Si NW piezoresistivity is the ideal transduction mechanism for replacing bulky counterparts such as capacitive displacement sensors. This is thanks to its well-understood principles of operation, immunity to noise, reduced power requirements, and ease of characterization and calibration. It provides an on-chip solution that can be integrated well with electronics. Various demonstrations of such integration are covered in this review. Comparison with commercial counterparts and historical evolution of a sensor type, where available, is provided. Significant technology development is necessary to eliminate fab-related variations and uncertainties that would affect the piezoresistive response through intrinsic stresses and surface effects.[164] For example, the effect of native oxide, a factor that is commonly ignored in bulk Si, becomes appreciable due to the dominant role played by the surface in NW mechanical behavior.[165] The developments in gate-all-around transistors pave the way for scalable production of free-standing Si structures at industry scale and will surely have a positive impact in the field of NEMS in the near future. 3) As in electronics, the miniaturization resulting from the integration of Si NWs provides double benefits. While a performance improvement (higher sensitivity, enhanced resolution, and better SNR) is achieved with Si NW strain gages, the parallel reduction of the overall chip size results in cost reduction. The existence of this cycle justifies the further investment for item (1) above regarding the technology development.

© 2023 The Authors. Advanced Engineering Materials published by Wiley-VCH GmbH

15272648, 2023, 12, Downloaded from https://onlinelibrary.wiley.com/doi/10.1002/adem.202300007 by Turkey Cochrane Evidence Aid, Wiley Online Library on [20/02/2025]. See the Terms and Conditions (https://onlinelibrary.wiley.com/terms-and-conditions) on Wiley Online Library for rules of use; OA articles are governed by the applicable Creative Commons License

A limited number of early attempts of utilizing Si NWs in MEMS physical sensors[166] reflects this potential. Similar visionary examples of early MEMS attempts of the 60 s[167] never reached commercial success, as enabling technologies such as IC technology and microfabrication of mechanical parts could not simply deliver the necessary support. However, with increased maturity on the technology front, such MEMS devices started finding application in the early 80 s,[168] with MEMS constituting a trillion-dollar market today. Therefore, both the challenges and intensity of research activity highlighted in this review fit the pattern of the evolution of the previous generation of semiconductor sensors.

In addition to technological maturity, much needs to be accomplished on the metrology front. With Si NWs serving as electromechanical components, a better understanding of their mechanical behavior is necessary. A look at the current literature reveals significant deviations among different characterization studies for even the simplest mechanical properties such as the modulus of elasticity.[169] While testing is quite challenging due to the smallness of dimensions and forces involved, the interpretation of testing results through multiscale models also poses a series of issues, thus contributing to the current spread of data in the literature. The same problem was encountered to a certain degree in MEMS as well, as exemplified by polySi.[170] However, the relatively large dimensions helped develop excellent fabrication and testing techniques and facilitated the use of relatively straightforward models. Hence, in less than a decade, a consensus could be established regarding the modulus of elasticity. However, for NEMS materials in general and for Si NWs in particular, such consensus will take much longer to achieve. To a large extent, device applications reviewed in this work will benefit from such an understanding at the fundamental level.

Acknowledgements

This work was supported by TÜBİTAK under grant numbers 120N361, 118C155, and 120E347.

Conflict of Interest

The authors declare no conflict of interest.

Keywords

deep etch, inertial sensors, microelectromechanical systems/nanoelectromechanical systems (MEMS/NEMS), piezoresistivity, single-crystal reactive etching and metallization (SCREAM), silicon nanowires, thin silicon-on-insulator (SOI)

Received: January 2, 2023
Revised: April 3, 2023
Published online: May 7, 2023

[1] K. L. Ekinci, *Small* **2005**, *1*, 786.
[2] W. Yu, Y. Liu, T. Dillon, W. Rahayu, F. Mostafa, *IEEE Internet Things J.* **2021**, *9*, 2443.
[3] B. Maag, Z. Zhou, L. Thiele, *IEEE Internet Things J.* **2018**, *5*, 4857.
[4] F. Wu, T. Wu, M. R. Yuce, in *IEEE 5th World Forum Internet Things, WF-IoT 2019 - Conf. Proc.*, IEEE, Piscataway, NJ **2019**, p. 87.
[5] M. S. Lundstrom, M. A. Alam, *Science* **2022**, *378*, 722.
[6] P. Ye, T. Ernst, V. M. Khare, *IEEE Spectr.* **2019**, *58*, 31.
[7] A. Rawat, P. Vardhan, U. Ganguly, *IEEE Nanotechnol. Mag.* **2020**, *14*, 4.
[8] R. Kapoor, R. Adner, *Solid State Technol.* **2007**, *50*, 51.
[9] E. P. Debenedictis, *Computer* **2017**, *50*, 72.
[10] W. E. Newell, *Science* **1968**, *161*, 1320.
[11] B. E. Alaca, M. Karimzadehkhouei, *Encyclopedia of Sensors and Biosensors*, Elsevier Inc., Amsterdam **2023**, p. 555.
[12] B. V. Schmidt, J. V. Wittemann, S. Senz, U. Go, *Adv. Mater.* **2009**, *21*, 2681.
[13] R. Rurali, *Rev. Mod. Phys.* **2010**, *82*, 427.
[14] Y. T. Yang, C. Callegari, X. L. Feng, K. L. Ekinci, M. L. Roukes, *Nano Lett.* **2006**, *6*, 583.
[15] O. M. Maragò, P. H. Jones, F. Bonaccorso, V. Scardaci, P. G. Gucciardi, A. G. Rozhin, A. C. Ferrari, *Nano Lett.* **2008**, *8*, 3211.
[16] A. K. Naik, M. S. Hanay, W. K. Hiebert, X. L. Feng, M. L. Roukes, *Nat. Nanotechnol.* **2009**, *4*, 445.
[17] I. Bargatin, E. B. Myers, J. S. Aldridge, C. Marcoux, P. Brianceau, L. Duraffourg, E. Colinet, S. Hentz, P. Andreucci, M. L. Roukes, *Nano Lett.* **2012**, *12*, 1269.
[18] P. Robert, V. Nguyen, S. Hentz, L. Duraffourg, G. Jourdan, J. Arcamone, S. Harrisson, in *Proc. IEEE Sensors*, IEEE, Piscataway, NJ **2009**, p. 963.
[19] M. Nasr Esfahani, Y. Leblebici, B. E. Alaca, *J. Microelectromech. Syst.* **2017**, *26*, 624.
[20] P. C. McIntyre, A. Fontcuberta i Morral, *Mater. Today Nano* **2020**, *9*, 100058.
[21] B. E. Alaca, *Int. Mater. Rev.* **2009**, *54*, 245.
[22] E. Gil-Santos, D. Ramos, J. Martínez, M. Ferníndez-Regúlez, R. García, Á. San Paulo, M. Calleja, J. Tamayo, *Nat. Nanotechnol.* **2010**, *5*, 641.
[23] M. Fernandez-Regulez, M. Sansa, M. Serra-Garcia, E. Gil-Santos, J. Tamayo, F. Perez-Murano, A. San Paulo, *Nanotechnology* **2013**, *24*, 095303.
[24] R. Singh, in *IEEE Electron Devices Society Newsletters*, IEEE, Piscataway, NJ **2015**, p. 13.
[25] S. Barth, F. Hernandez-Ramirez, J. D. Holmes, A. Romano-Rodriguez, *Prog. Mater. Sci.* **2010**, *55*, 563.
[26] F. Wang, A. Dong, W. E. Buhro, *Chem. Rev.* **2016**, *116*, 10888.
[27] N. P. Dasgupta, J. Sun, C. Liu, S. Brittman, S. C. Andrews, J. Lim, H. Gao, R. Yan, P. Yang, *Adv. Mater.* **2014**, *26*, 2137.
[28] K. A. Shaw, Z. L. Zhang, N. C. MacDonald, *IEEE Micro Electro Mech. Syst.* **1994**, *40*, 155.
[29] N. C. MacDonald, *Microelectron. Eng.* **1996**, *32*, 49.
[30] K. A. Shaw, N. C. MacDonald, in *Proc. IEEE Micro Electro Mechanical System*, IEEE, Piscataway, NJ **1996**, p. 44.
[31] A. Jazairy, N. C. MacDonald, *Microelectron. Eng.* **1996**, *30*, 527.
[32] M. T. A. Saif, N. C. MacDonald, *Sens. Actuators, A* **1996**, *52*, 65.
[33] M. T. A. Saif, N. C. MacDonald, *J. Microelectromech. Syst.* **1996**, *5*, 79.
[34] R. Y. Webb, S. G. Adams, N. C. MacDonald, *Microrobotics and Micromanipulation*, Vol. *3519*, Wiley-ISTE, London **1998**, p. 196.
[35] W. Hofmann, C. S. Lee, N. C. MacDonald, *Sens. Mater.* **1998**, *10*, 337.
[36] J. M. Chen, N. C. MacDonald, *Rev. Sci. Instrum.* **2004**, *75*, 276.
[37] K. T. Park, H. C. Kim, K. Chun, in *Proc. - 1st Int. Conf. Sensor Device Technologies and Applications SENSORDEVICES 2010*, Venice, Italy **2010**, p. 246.
[38] T. Tsuchiya, T. Hemmi, J. Y. Suzuki, Y. Hirai, O. Tabata, *Procedia Struct. Integrity* **2016**, *2*, 1405.
[39] Z. Tasdemir, O. Peric, D. Sacchetto, G. E. Fantner, Y. Leblebici, B. E. Alaca, *IEEE Trans. Nanotechnol.* **2018**, *17*, 1299.
[40] T. Kim, S. Jang, B. Chang, J. Sung, S. Lee, H. Ko, K. Koo, D. D. Cho, in *2019 20th Int. Conf. Solid-State Sensors, Actuators Microsystems*

© 2023 The Authors. Advanced Engineering Materials published by Wiley-VCH GmbH

15272648, 2023, 12, Downloaded from https://onlinelibrary.wiley.com/doi/10.1002/adem.202300007 by Turkey Cochrane Evidence Add, Wiley Online Library on [20/02/2025]. See the Terms and Conditions (https://onlinelibrary.wiley.com/terms-and-conditions) on Wiley Online Library for rules of use; OA articles are governed by the applicable Creative Commons License

Eurosensors XXXIII (Transducers Eurosensors XXXIII), Berlin, Germany **2019**, p. 1949.
[41] J. J. Yao, S. C. Arney, N. C. MacDonald, *J. Microelectromech. Syst.* **1992**, *1*, 14.
[42] W. Zhang, W. Zhang, K. Turner, P. G. Hartwell, in *Proc. IMECE04 2004 ASME Int. Mechanical Engineering Congress and Exposition*, Anaheim, CA **2004**, p. 1.
[43] Z. Tasdemir, N. Wollschläger, W. Österle, Y. Leblebici, B. E. Alaca, *Nanotechnology* **2016**, *27*, 095303.
[44] M. Nasr Esfahani, M. Yilmaz, N. Wollschläger, I. W. Rangelow, Y. Leblebici, B. E. Alaca, *Microelectron. Eng.* **2017**, *183–184*, 42.
[45] T. Nakamura, Y. Hirai, O. Tabata, T. Tsuchiya, in *Proc. IEEE Int. Conf. Micro Electro Mechanical Systems*, IEEE, Piscataway, NJ, January 2020, p. 1157.
[46] M. Yilmaz, Y. Kilinc, G. Nadar, Z. Tasdemir, N. Wollschläger, W. Österle, Y. Leblebici, B. E. Alaca, *J. Vac. Sci. Technol., B: Nanotechnol. Microelectron.: Mater., Process., Meas., Phenom.* **2017**, *35*, 022001.
[47] H. Zou, J. Wang, F. Chen, H. Bao, D. Jiao, K. Zhang, Z. Song, X. Li, *J. Micromech. Microeng.* **2017**, *27*, 075009.
[48] J. Van Schoot, H. Schift, *Adv. Opt. Technol.* **2017**, *6*, 159.
[49] R. Fallica, D. Kazazis, R. Kirchner, A. Voigt, I. Mochi, H. Schift, Y. Ekinci, *J. Vac. Sci. Technol., B: Nanotechnol. Microelectron.: Mater., Process., Meas., Phenom.* **2017**, *35*, 061603.
[50] L. Weidenfeller, M. Hofmann, S. Supreeti, S. Mechold, M. Holz, C. Reuter, E. Manske, I. W. Rangelow, *Microelectron. Eng.* **2020**, *227*, 111325.
[51] Y. M. Georgiev, N. Petkov, B. McCarthy, R. Yu, V. Djara, D. O'Connell, O. Lotty, A. M. Nightingale, N. Thamsumet, J. C. Demello, A. Blake, S. Das, J. D. Holmes, *Microelectron. Eng.* **2014**, *118*, 47.
[52] N. Wollschläger, Z. Tasdemir, I. Häusler, Y. Leblebici, W. Österle, B. E. Alaca, *J. Nanomater.* **2016**, 1, article no. 4905838.
[53] S. Dolabella, R. Frison, G. A. Chahine, C. Richter, T. U. Schulli, Z. Tasdemir, B. E. Alaca, Y. Leblebici, A. Dommann, A. Neels, *J. Appl. Crystallogr.* **2020**, *53*, 58.
[54] J. M. Lee, C. U. Jang, C. J. Choi, K. B. Kwon, J. S. Han, N. Y. Kwon, J. S. Ko, *Int. J. Precis. Eng. Manuf.* **2016**, *17*, 637.
[55] I. L. Berry, A. L. Caviglia, *J. Vac. Sci. Technol., B: Microelectron. Nanometer Struct.* **1983**, *1*, 1059.
[56] J. Brugger, G. Beljakovic, M. Despont, N. F. de Rooij, P. Vettiger, *Microelectron. Eng.* **1997**, *35*, 401.
[57] L. Bischoff, B. Schmidt, H. Lange, D. Donzev, *Nucl. Instrum. Methods Phys. Res., Sect. B* **2009**, *267*, 1372.
[58] R. Böttger, L. Bischoff, B. Schmidt, M. Krause, *J. Micromech. Microeng.* **2011**, *21*, 095025.
[59] J. Llobet, M. Sansa, M. Gerbolés, N. Mestres, J. Arbiol, X. Borrisé, F. Pérez-Murano, *Nanotechnology* **2014**, *25*, 135302.
[60] J. Llobet, M. Sansa, M. Lorenzoni, X. Borrisé, A. San Paulo, F. Pérez-Murano, *Appl. Phys. Lett.* **2015**, *107*, 073104.
[61] J. Llobet, M. Gerbolés, M. Sansa, J. Bausells, X. Borrisé, F. Perez-Murano, *J. Micro/Nanolithogr., MEMS, MOEMS* **2015**, *14*, 031207.
[62] J. Llobet, E. Krali, C. Wang, J. Arbiol, M. E. Jones, F. Pérez-Murano, Z. A. K. Durrani, *Appl. Phys. Lett.* **2015**, *107*, 223501.
[63] M. Lorenzoni, J. Llobet, F. Gramazio, M. Sansa, J. Fraxedas, F. Perez-Murano, *J. Vac. Sci. Technol., B: Nanotechnol. Microelectron.: Mater., Process., Meas., Phenom.* **2016**, *34*, 06KK02.
[64] J. Llobet, G. Rius, A. Chuquitarqui, X. Borrisé, R. Koops, M. Van Veghel, F. Perez-Murano, *Nanotechnology* **2018**, *29*, 155303.
[65] M. Lorenzoni, J. Llobet, F. Perez-Murano, *Appl. Phys. Lett.* **2018**, *112*, 193102.
[66] V. Tzanov, J. Llobet, F. Torres, F. Perez-Murano, N. Barniol, *Nanomaterials* **2020**, *10*, 811.
[67] P. Sievila, N. Chekurov, I. Tittonen, *Nanotechnology* **2010**, *21*, 145301.
[68] G. Rius, J. Llobet, X. Borrisé, N. Mestres, A. Retolaza, S. Merino, F. Perez-Murano, *J. Vac. Sci. Technol., B: Microelectron. Nanometer Struct.* **2009**, *27*, 2691.
[69] N. Chekurov, K. Grigoras, L. Sainiemi, A. Peltonen, I. Tittonen, S. Franssila, *J. Micromech. Microeng.* **2010**, *20*, 085009.
[70] D. Ettelt, G. Dodane, M. Audoin, A. Walther, G. Jourdan, P. Rey, P. Robert, J. Delamare, in *Proc. IEEE Sensors*, IEEE, Piscataway, NJ **2011**, p. 2010.
[71] F. Souchon, L. Joet, C. Ladner, P. Rey, S. Louwers, in *Proc. IEEE Sensors*, IEEE, Piscataway, NJ, October 2019.
[72] T. Miani, T. Verdot, A. Berthelot, F. Maspero, A. Koumela, P. Robert, G. Langfelder, J. Arcamone, M. Sansa, in *Proc. IEEE Int. Conf. Micro Electro Mechanical Systems*, IEEE, Piscataway, NJ **2021**, p. 192.
[73] M. Gadola, A. Buffoli, M. Sansa, A. Berthelot, P. Robert, G. Langfelder, *J. Microelectromech. Syst.* **2021**, *30*, 513.
[74] A. A. Barlian, W. T. Park, J. R. Mallon, A. J. Rastegar, B. L. Pruitt, *Proc. IEEE* **2009**, *97*, 513.
[75] N. Yazdi, F. Ayazi, K. Najafi, *Proc. IEEE* **1998**, *86*, 1640.
[76] V. Narasimhan, H. Li, M. Jianmin, *J. Micromech. Microeng.* **2015**, *25*, 033001.
[77] F. Maspero, S. Delachanal, A. Berthelot, L. Joet, G. Langfelder, S. Hentz, *IEEE Sens. J.* **2020**, *20*, 689.
[78] J. Zhao, X. Wang, Y. Zhao, G. M. Xia, A. P. Qiu, Y. Su, Y. P. Xu, *IEEE J. Solid-State Circuits* **2017**, *52*, 1053.
[79] T. Miani, F. Maspero, G. Langfelder, T. Verdot, A. Koumela, J. Arcamone, A. Berthelot, P. Robert, M. Sansa, in *2022 IEEE Int. Symp. Inertial Sensors and Systems*, IEEE, Piscataway, NJ **2022**, p. 1.
[80] B. Fain, A. Chaehoi, A. Berthelot, T. Verdot, F. Souchon, S. Delachanal, A. Koumela, A. Nowodzinski, H. Lhermet, G. Jourdan, P. Rey, P. Robert, in *Transducers 2017 - 19th Int. Conf. Solid-State Sensors, Actuators Microsystems*, Kaohsiung, Taiwan **2017**, p. 603.
[81] B. Fain, F. Souchon, A. Berthelot, R. Anciant, P. Robert, G. Jourdan, in *Proc. IEEE Int. Conf. Micro Electro Mechanical Systems*, IEEE, Piscataway, NJ, January 2018, p. 948.
[82] B. Fain, F. Souchon, A. Berthelot, R. Anciant, P. Robert, G. Jourdan, in *5th IEEE Int. Symp. Inertial Sensors and Systems Inertial 2018 - Proc.*, IEEE, Piscataway, NJ **2018**, p. 1.
[83] J. Liu, Y. Shi, P. Li, J. Tang, R. Zhao, H. Zhang, *Sens. Actuators, A* **2012**, *173*, 1.
[84] R. Kuells, S. Nau, M. Salk, K. Thoma, *Sens. Actuators, A* **2012**, *182*, 41.
[85] K. Fan, L. Che, B. Xiong, Y. Wang, *J. Micromech. Microeng.* **2007**, *17*, 1206.
[86] J. Dong, X. Li, Y. Wang, D. Lu, S. Ahat, *J. Micromech. Microeng.* **2002**, *12*, 742.
[87] P. Dong, X. Li, H. Yang, H. Bao, W. Zhou, S. Li, S. Feng, *Sens. Actuators, A* **2008**, *141*, 339.
[88] C. Jia, Q. Mao, G. Luo, L. Zhao, D. Lu, P. Yang, M. Yu, C. Li, B. Chang, Z. Jiang, *Rev. Sci. Instrum.* **2020**, *91*, 085001.
[89] Y. Ning, Y. Loke, G. McKinnon, *Sens. Actuators, A* **1995**, *48*, 55.
[90] K. M. Bae, J. M. Lee, K. B. Kwon, K. H. Han, N. Y. Kwon, J. S. Han, J. S. Ko, *J. Mech. Sci. Technol.* **2014**, *28*, 1449.
[91] S. Huang, X. Li, Z. Song, Y. Wang, H. Yang, L. Che, J. Jiao, *J. Micromech. Microeng.* **2005**, *15*, 993.
[92] V. G. Peshekhonov, *Gyroscopy Navig.* **2011**, *2*, 111.
[93] M. S. Weinberg, A. Kourepenis, *J. Microelectromech. Syst.* **2006**, *15*, 479.
[94] J. L. Chen, Y. N. Dai, N. S. Grimaldi, J. J. Lin, B. Y. Hu, Y. F. Wu, S. Gao, *Adv. Mater. Technol.* **2022**, *7*, 2100566.
[95] C. Acar, A. R. Schofield, A. A. Trusov, L. E. Costlow, A. M. Shkel, *IEEE Sens. J.* **2009**, *9*, 1895.
[96] A. Walther, M. Savoye, G. Jourdan, P. Renaux, F. Souchon, P. Robert, C. Le Blanc, N. Delorme, O. Gigan, C. Lejuste, in *Proc. IEEE Int. Conf. Micro Electro Mechanical Systems*, IEEE, Piscataway, NJ **2012**, p. 480.

© 2023 The Authors. Advanced Engineering Materials published by Wiley-VCH GmbH

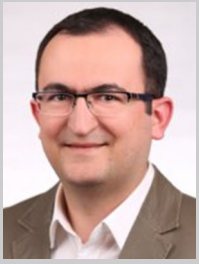
15272648, 2023, 12, Downloaded from https://onlinelibrary.wiley.com/doi/10.1002/adem.202300007 by Turkey Cochrane Evidence Aid, Wiley Online Library on [20/02/2025]. See the Terms and Conditions (https://onlinelibrary.wiley.com/terms-and-conditions) on Wiley Online Library for rules of use; OA articles are governed by the applicable Creative Commons License

[97] Y. Mochida, M. Tamura, K. Ohwada, *Sens. Actuators, A* **2000**, *80*, 170.
[98] S. Dellea, F. Giacci, A. Longoni, P. Rey, A. Berthelot, G. Langfelder, in *Proc. IEEE Int. Conf. Micro Electro Mechanical Systems*, IEEE, Piscataway, NJ **2015**, p. 37.
[99] S. Dellea, F. Giacci, A. F. Longoni, G. Langfelder, *J. Microelectromech. Syst.* **2015**, *24*, 1817.
[100] S. Dellea, F. Giacci, A. F. Longoni, G. Langfelder, P. Rey, P. Robert, in *IEEE 3rd Int. Symp. Inertial Sensors and Systems ISS 2016 - Proc.*, IEEE, Piscataway, NJ **2016**, p. 25.
[101] F. Giacci, S. Dellea, A. F. Longoni, G. Langfelder, in *2015 Transducers - 2015 18th Int. Conf. Solid-State Sensors, Actuators Microsystems, Transducers 2015*, Anchorage, AK **2015**, p. 780.
[102] A. Nikas, O. Leman, H. Zhou, J. L. Lagos, B. J. Vinchhi, J. Hauer, *Proc. - IEEE Int. Symp. Circuits and Systems*, IEEE, Piscataway, NJ, July 2016, p. 2238.
[103] S. Dellea, F. Giacci, P. Rey, A. Capodici, G. Langfelder, in *2016 IEEE 29th Int. Conf. Micro Electro Mechanical Systems*, IEEE, Piscataway, NJ **2016**, p. 255.
[104] F. Giacci, S. Dellea, G. Langfelder, *Microelectron. Reliab.* **2017**, *75*, 59.
[105] S. Dellea, P. Rey, G. Langfelder, *J. Microelectromech. Syst.* **2017**, *26*, 1389.
[106] S. Dellea, G. S. Strazzeri, P. Rey, G. Langfelder, in *Proc. IEEE Int. Conf. Micro Electro Mechanical Systems*, Vol. *1195*, IEEE, Piscataway, NJ **2017**, p. 21.
[107] E. Tatar, S. E. Alper, T. Akin, in *Proc. IEEE Int. Conf. Micro Electro Mechanical Systems*, IEEE, Piscataway, NJ **2011**, p. 569.
[108] S. Dellea, A. Longoni, G. Langfelder, A. Nikas, O. Leman, J. Hauer, G. Mantini, R. Naschberger, P. Rey, in *4th IEEE Int. Symp. Inertial Sensors and Systems Inertial 2017 - Proc.*, IEEE, Piscataway, NJ **2017**, p. 1.
[109] M. Gadola, M. Malvicini, G. Langfelder, M. Colin, P. Robert, in *Inertial 2019 - 6th IEEE Int. Symp. Inertial Sensors and Systems Proc.*, IEEE, Piscataway, NJ **2019**, p. 2.
[110] M. Gadola, F. Maspero, G. Langfelder, M. Sansa, T. Verdot, A. Berthelot, P. Robert, *Proc. IEEE Sensors*, IEEE, Piscataway, NJ, October 2020, p. 3.
[111] M. Gadola, M. S. Perna, M. Allieri, P. Robert, T. Verdot, A. Berthelot, G. Langfelder, in *2021 IEEE Int. Symp. Inertial Sensors and Systems*, IEEE, Piscataway, NJ **2021**, p. 1.
[112] ReportLinker Consulting Market Reports, February 2023, https://www.reportlinker.com/p06249264/MEMS-Pressure-Sensors-Market-Growth-Trends-COVID-19-Impact-and-Forecasts.html.
[113] P. Song, Z. Ma, J. Ma, L. Yang, J. Wei, Y. Zhao, M. Zhang, F. Yang, X. Wang, *Micromachines* **2020**, *11*, 56.
[114] J. C. Doll, B. L. Pruitt, *Piezoresistor Design and Applications*, Springer New York **2013**.
[115] N. Maluf, *An Introduction to MEMS Engineering*, Artech House Publishers, Norwood **2004**.
[116] J. H. Kim, K. T. Park, H. C. Kim, K. Chun, in *Transducers 2009 - 15th Int. Conf. Solid-State Sensors, Actuators Microsystems*, Denver, CO **2009**, p. 1936.
[117] J. Zhang, Y. Zhao, Y. Ge, M. Li, L. Yang, X. Mao, *Micromachines* **2016**, *7*, 187.
[118] P. Rey, A. Berthelot, G. Jourdan, H. Duchemin, R. Anciant, H. Blanc, P. Robert, in *2016 IEEE 29th Int. Conf. Micro Electro Mechanical Systems*, IEEE, Piscataway, NJ **2016**, p. 846.
[119] A. Koumela, P. Brunet-Manquat, L. Joët, A. Berthelot, P. Rey, *Microelectron. Reliab.* **2020**, *114*, 113805.
[120] B. W. Soon, P. Neuzil, C. C. Wong, J. Reboud, H. H. Feng, C. Lee, *Procedia Eng.* **2010**, *5*, 1127.
[121] L. S. Lim, W. T. Park, L. Lou, H. H. Feng, P. Singh, *Adv. Mater. Res.* **2011**, *254*, 94.
[122] L. Lou, S. Zhang, W. T. Park, J. M. Tsai, D. L. Kwong, C. Lee, *J. Micromech. Microeng.* **2012**, *22*, 055012.
[123] S. Zhang, T. Wang, L. Lou, W. M. Tsang, R. Sawada, D. L. Kwong, C. Lee, *J. Microelectromech. Syst.* **2014**, *23*, 1396.
[124] S. Zhang, L. Lou, Y. A. Gu, *IEEE Electron Device Lett.* **2017**, *38*, 653.
[125] J. Tiete, F. Domínguez, B. da Silva, A. Touhafi, K. Steenhaut, *Wireless MEMS Networks and Applications*, Woodhead Publishing, Sawston **2017**, p. 177.
[126] S. A. Zawawi, A. A. Hamzah, B. Y. Majlis, F. Mohd-Yasin, *Micromachines* **2020**, *11*, 484.
[127] J. Czarny, *Conception, Fabrication and Characterization of a MEMS Microphone*, L'institut national des sciences appliques de Lyon, Villeurbanne **2015**.
[128] F. Pfiffner, L. Prochazka, D. Peus, I. Dobrev, A. Dalbert, J. H. Sim, R. Kesterke, J. Walraevens, F. Harris, C. Roosli, D. Obrist, A. Huber, *IEEE Trans. Biomed. Eng.* **2017**, *64*, 2431.
[129] J. Bay, O. Hansen, S. Bouwstra, *Sens. Actuators, A* **1996**, *53*, 232.
[130] Z. Wang, Q. Zou, Q. Song, J. Tao, in *2015 Transducers - 2015 18th Int. Conf. Solid-State Sensors, Actuators Microsystems*, IEEE, Piscataway, NJ **2015**, p. 375.
[131] H. Lhermet, T. Verdot, A. Berthelot, B. Desloges, F. Souchon, in *Proc. IEEE Int. Conf. Micro Electro Mechanical Systems*, IEEE, Piscataway, NJ **2018**, p. 249.
[132] H. Lhermet, T. Verdot, A. Teulle, A. Berthelot, A. Gliere, B. Desloges, F. Souchon, M. Fournier, J. Fédéli, J. Coutard, in *2019 20th Int. Conf. Solid-State Sensors, Actuators Microsystems Eurosensors XXXIII (Transducers Eurosensors XXXIII)*, Berlin, Germany **2019**, p. 68.
[133] J. Nebhen, E. Savary, W. Rahajandraibe, C. Dufaza, S. Meillere, F. Haddad, E. Kussener, H. Barthelemy, J. Czarny, A. Walther, in *Proc. IEEE Int. Conf. Electronics, Circuits and Systems*, IEEE, Piscataway, NJ **2013**, p. 445.
[134] C. Guianvarc'h, T. Verdot, J. Czarny, E. Redon, K. Ege, J. L. Guyader, A. Walther, P. Robert, in *Proc. Meetings on Acoustics*, Montreal, Canada **2013**.
[135] J. Czarny, T. Verdot, E. Redon, A. Walther, H. Lhermet, B. Desloges, K. Ege, P. Robert, J.-L. Guyader, in *12ème Congrès Français d'Acoustique CFA 2014*, Poitiers, France **2014**, p. 189.
[136] T. Verdot, E. Redon, K. Ege, J. Czarny, C. Guianvarc'h, J. L. Guyader, *Acta Acust. United Acust.* **2016**, *102*, 517.
[137] J. Nebhen, E. Savary, W. Rahajandraibe, C. Dufaza, S. Meillere, E. Kussener, H. Barthelemy, J. Czarny, A. Walther, in *Proc. IEEE Sensors*, IEEE, Piscataway, NJ **2013**, p. 4.
[138] E. Savary, W. Rahajandraibe, S. Meillère, E. Kussener, H. Barthelemy, J. Czarny, H. Lhermet, P. Robert, in *2014 21st IEEE Int. Conf. Electronics, Circuits and Systems ICECS 2014*, IEEE, Piscataway, NJ **2014**, p. 558.
[139] J. Nebhen, P. M. Ferreira, S. Mansouri, *J. Low Power Electron. Appl.* **2020**, *10*, 13.
[140] S. Lee, B. Chang, T. Kim, A. Jin, D. Il Dan Cho, *Int. Conf. Control Autom. Syst.* **2019**, *2019*, 1685.
[141] G. Baldini, F. Dimc, R. Kamnik, G. Steri, R. Giuliani, C. Gentile, *Sensors* **2017**, *17*, 783.
[142] S. Jeong, S. Kuk, H. Kim, *IEEE Access* **2019**, *7*, 20734.
[143] InvenSense Products https://invensense.tdk.com/products/motion-tracking/9-axis/mpu-9150-2/.
[144] D. Ettelt, P. Rey, G. Jourdan, A. Walther, P. Robert, J. Delamare, *J. Microelectromech. Syst.* **2014**, *23*, 324.
[145] M. J. Thompson, M. Li, D. A. Horsley, in *Proc. IEEE Int. Conf. Micro Electro Mechanical Systems*, IEEE, Piscataway, NJ **2011**, p. 593.
[146] F. Ejeian, S. Azadi, A. Razmjou, Y. Orooji, A. Kottapalli, M. Ebrahimi Warkiani, M. Asadnia, *Sens. Actuators, A* **2019**, *295*, 483.
[147] S. Silvestri, E. Schena, *Micromachines* **2012**, *3*, 225.
[148] J. T. W. Kuo, L. Yu, E. Meng, *Micromachines* **2012**, *3*, 550.
[149] Y. H. Wang, C. Y. Lee, C. M. Chiang, *Sensors* **2007**, *7*, 2389.
[150] B. Idjeri, M. Laghrouche, J. Boussey, *IEEE Sens. J.* **2017**, *17*, 4181.

© 2023 The Authors. Advanced Engineering Materials published by Wiley-VCH GmbH

15272648, 2023, 12, Downloaded from https://onlinelibrary.wiley.com/doi/10.1002/adem.202300007 by Turkey Cochrane Evidence Add, Wiley Online Library on [20/02/2025]. See the Terms and Conditions (https://onlinelibrary.wiley.com/terms-and-conditions) on Wiley Online Library for rules of use; OA articles are governed by the applicable Creative Commons License

[151] V. Balakrishnan, T. Dinh, H. P. Phan, D. V. Dao, N. T. Nguyen, *Sens. Actuators, A* **2018**, *279*, 293.
[152] S. Kim, T. Nam, S. Park, *Sens. Actuators, A* **2004**, *114*, 312.
[153] H. Berthet, J. Jundt, J. Durivault, B. Mercier, D. Angelescu, *Lab Chip* **2011**, *11*, 215.
[154] Q. Zhang, W. Ruan, H. Wang, Y. Zhou, Z. Wang, L. Liu, *Sens. Actuators, A* **2010**, *158*, 273.
[155] S. Zhang, L. Lou, W. T. Park, C. Lee, *J. Micromech. Microeng.* **2012**, *22*.
[156] Y. Xu, C. W. Chiu, F. Jiang, Q. Lin, Y. C. Tai, *Sens. Actuators, A* **2005**, *121*, 253.
[157] L. Lofdahl, G. Stemme, B. Johansson, *J. Phys. E* **1989**, *22*, 391.
[158] R. Buchner, C. Sosna, M. Maiwald, W. Benecke, W. Lang, *Sens. Actuators, A* **2006**, *130–131*, 262.
[159] N. T. Nguyen, *Flow Meas. Instrum.* **1997**, *8*, 7.
[160] C. Sosna, T. Walter, W. Lang, *Sens. Actuators, A* **2011**, *172*, 15.
[161] D. Li, T. Zhao, Z. Yang, D. Zhang, *J. Micromech. Microeng.* **2010**, *20*, 035024.
[162] C. Y. Lee, C. Y. Wen, H. H. Hou, R. J. Yang, C. H. Tsai, L. M. Fu, *Microfluid. Nanofluidics* **2009**, *6*, 363.
[163] R. H. Ma, C. Y. Lee, Y. H. Wang, H. J. Chen, *Microsyst. Technol.* **2008**, *14*, 971.
[164] S. Zare Pakzad, M. Nasr Esfahani, B. E. Alaca, *Mater. Today Commun.* **2023**, *34*, 105002.
[165] M. Nasr Esfahani, S. Zare Pakzad, T. Li, X. Li, Z. Tasdemir, N. Wollschläger, Y. Leblebici, B. E. Alaca, *ACS Appl. Nano Mater.* **2022**, *5*, 13276.
[166] Commercial Micro Manufacturing International magazine, February 2014, http://www.cmmmagazine.com/mems/tronics-manufactures-the-first-piezoresistive-nanowire-6dof-/.
[167] H. C. Nathanson, R. A. Wickstrom, *Appl. Phys. Lett.* **1965**, *7*, 84.
[168] R. T. Howe, R. S. Muller, *IEEE Trans. Electron Devices* **1986**, *33*, 499.
[169] M. Nasr Esfahani, B. E. Alaca, *Adv. Eng. Mater.* **2019**, *21*, 1.
[170] K. J. Hemker, W. N. Sharpe, *Annu. Rev. Mater. Res.* **2007**, *37*, 92.



Mehrdad Karimzadehkhouei received his B.S. and M.S. degrees in mechanical engineering from Urmia University, Iran, and Istanbul Technical University, Turkey, in 2007 and 2012, respectively, and his Ph.D. degree in mechatronics engineering from Sabancı University, Turkey, in 2017. He joined Koç University Mechanical Engineering Program as a Research Associate in 2019, Mechanical Characterization Laboratory (MCL). He worked on nanoscale heat and mass transfer during his Ph.D. and microfabrication, and microfluidics during his postdoctoral period in Micro-Nano Scale Heat Transfer and Microfluidics Research Group, Sabancı University. Dr. Karimzadehkhouei is currently working on MEMS/NEMS design and Si nanowire-based sensors (https://orcid.org/0000-0002-2712-1908).



Basit Ali graduated with a B.E. degree in aerospace engineering from the National University of Sciences & Technology, Islamabad and joined Mechanical Characterization Laboratory at Koç University in 2020 as a direct Ph.D. student. Currently, he is pursuing his Ph.D. in the Department of Mechanical Engineering. His research interest lies in the field of NEMS and silicon nanowire-based piezoresistive sensors (https://orcid.org/0000-0003-2063-1566).



Masoud Jedari Ghourichaei received his B.S. degree in mechanical engineering from the University of Tabriz in 2014. After receiving his M.Sc. degree from the Sahand University of Technology, he joined MCL in Spring of 2020. Currently, he is working on the fabrication and characterization of M&NEMS sensors. His research interest is in the field of high-performance MEMS sensors with Si nanowire transducers (https://orcid.org/0000-0002-7702-0566).



Burhanettin Erdem Alaca received his B.S. degree in mechanical engineering from Boğaziçi University, Istanbul, Turkey, in 1997, and his M.S. and Ph.D. degrees in mechanical engineering from the University of Illinois at Urbana–Champaign in 1999 and 2003, respectively. He joined Koç University in 2004, where he is currently a professor of mechanical engineering serving as the PI of Mechanical Characterization Laboratory (MCL). His research interests include mechanical behavior at the small-scale, micro and nanofabrication technologies and precision instruments based on nanoelectromechanical devices. He is a member of the Turkish National Committee on Theoretical and Applied Mechanics and IEEE (https://orcid.org/0000-0001-5931-8134).

© 2023 The Authors. Advanced Engineering Materials published by Wiley-VCH GmbH

15272648, 2023, 12, Downloaded from https://onlinelibrary.wiley.com/doi/10.1002/adem.202300007 by Turkey Cochrane Evidence Aid, Wiley Online Library on [20/02/2025]. See the Terms and Conditions (https://onlinelibrary.wiley.com/terms-and-conditions) on Wiley Online Library for rules of use; OA articles are governed by the applicable Creative Commons License